

Decadal in-situ hydrological observations and empirical modeling of pressure head in a high-alpine, fractured calcareous rock slope

Riccardo Scandroglio¹, Samuel Weber^{2,3}, Till Rehm⁴, and Michael Krautblatter¹

¹Landslide Research Group, TUM School of Engineering and Design, Technical University of Munich, Munich, Germany

²WSL Institute for Snow and Avalanche Research SLF, Davos Dorf, Switzerland

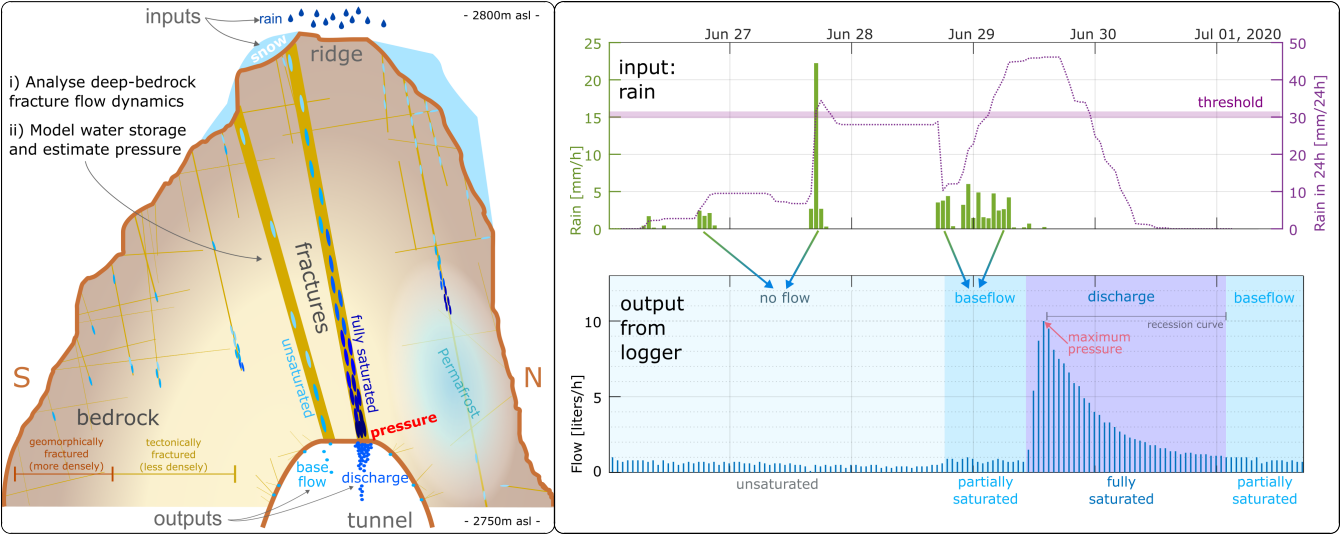
³Climate Change, Extremes and Natural Hazards in Alpine Regions Research Center, CERC, Davos Dorf, Switzerland

⁴Environmental Research Station Schneefernerhaus, Zugspitze, Germany

Correspondence: Riccardo Scandroglio (r.scandroglio@tum.de)

Abstract

In peri- and paraglacial regions, water plays a critical role in the hydrological cycle and slope stability. However, hydrological models often overlook water infiltration into bedrock due to limited knowledge of groundwater dynamics at high elevations. Although the link between water presence and rock slope failures is evident in many cases, proof of hydrostatic pressure buildup at depth is scarce, highlighting another significant research gap. This study aims to decipher the hydrological dynamics and empirically derive hydrostatic pressures in deep bedrock. We present unique decennial meteorological data, snowmelt modeling, and discharge measurements from two rock fractures in a tunnel located at ≈ 55 m depth under the permafrost-affected Zugspitze Ridge (2815-2962 m asl). We developed an empirical hydraulic model and detected flow anomalies by comparing inputs (i.e., snowmelt and rainfall) and outputs (i.e., discharge from fractures, baseflow, and no-flow events). Results show continuous flow during snowmelt and discontinuous events during summer months. Hydraulic conductivities are in the order of 10^{-4} m/s, with variations according to the saturation. Extreme events are likely to fully saturate the fractures and increase their interconnectivity, producing discharges up to 800 l/d and 58 l/h from one single fracture. Hydrostatic pressures calculated implementing Darcy’s falling-head law are 27 ± 6 m during average snowmelt and 40 ± 10 m for extreme events. These pressure levels can weaken or even destabilize rock slopes in rapidly warming alpine environments. With ongoing climate changes, water relevance is expected to increase, with impacts that yet have to be fully assessed. This study advances the understanding of alpine hydrology and geomorphology by providing new insights into deep groundwater processes and their implications for slope stability.



. Graphical abstract. Left: relevant geomorphological and hydraulic components. Right: input and output measurements.

1 Introduction

High mountain regions are recognized as “global water towers” (Viviroli et al., 2007), significantly contributing to water resources for approximately 1.9 billion people (Immerzeel et al., 2020). During periods of limited recharge, alpine groundwater becomes particularly important, providing up to 50% of adjacent lowland aquifers (Markovich et al., 2019; Hayashi, 2020). Groundwater flow within mountain bedrock can be categorized into two distinct components. The primary flow occurs at shallow depths and is predominantly driven by topography (Clarke and Burbank, 2011; Welch and Allen, 2014). The secondary flow is deeper and exhibits greater complexity: it is controlled by fracture density, geometry, and connectivity (Banks et al., 2009) as well as a decrease in permeability with depth (Manning and Caine, 2007).

While measurements with lysimeters focus on shallow flow (Courtin and Bliss, 1971; Rist and Phillips, 2005), there is a considerable lack of knowledge about deep groundwater dynamics in alpine slopes and their connection with the cryosphere (van Tiel et al., 2024). Direct measurements of deep groundwater in fractured alpine bedrock using wells are limited to a few studies (Manning and Caine, 2007; Gabrielli et al., 2012) due to the logistical challenges of rugged terrain, harsh weather conditions, and significant spatial variability (Walvoord and Kurylyk, 2016; Arenson et al., 2022). Piezometric measurements in fractures or boreholes are mostly of difficult interpretation (Draebing et al., 2017; Phillips et al., 2023; Bast et al., 2024), while combined geophysical methods can identify liquid water presence (Hauck et al., 2011; Watlet et al., 2018; Pavoni et al., 2023), but cannot measure pressure. So far, studies on high-alpine hydrology have predominantly focused on talus slopes, moraines, or rock glaciers (Hayashi, 2020; Noetzli and Phillips, 2019; Jones et al., 2018; Arenson et al., 2022) and only recently, Ben-Asher et al. (2023) modeled surface hydrological fluxes in steep bedrock permafrost.

In these environments, water presence also influences slope stability, as shown in numerous failure events (Fischer et al., 2010; Stoffel and Huggel, 2012; Walter et al., 2020; Kristensen et al., 2021) where hydrostatic pressure has been hypothesized as one of the destabilizing factors. In the theoretical model by Krautblatter et al. (2013), hydrostatic pressure can destabilize slopes by increasing lateral shear stress, decreasing frictional strength, and reducing normal stress. Mechanical simulations at slope scale confirm the critical role of water within fractures for stability (Scandroglio et al., 2021; Magnin and Josnin, 2021). From the thermal point of view, water percolating in fractures can quickly thaw bedrock by advection and, therefore, destabilize larger rock masses than heat conduction (Haeberli et al., 1997; Gruber and Haeberli, 2007). Still, so far, direct field evidence of thermal disturbance at depth is only available for one site (Phillips et al., 2016).

Despite the critical role of fracture water in alpine environments, there is a lack of reliable data and modeling efforts, resulting in an inadequate understanding of groundwater flow dynamics and little knowledge of hydrostatic pressures at depth. To address these two gaps, we present a decade-long dataset of high-alpine fracture discharge measurements at significant depths. First, we investigate the spatial and temporal patterns of water flow in deep bedrock fractures in response to snowmelt and rainfall events. Then, we develop an empirical model of fracture water dynamics to constrain catchment characteristics and identify periods of water accumulation. Finally, we provide innovative estimates of hydrostatic pressures in a high-alpine, fractured calcareous rock slope.

2 Study site

Measurements took place on Mount Zugspitze (2962 m asl, Fig. 1a), located in the Northern Calcareous Alps at the German-Austrian border. The study site is located southwest of the summit, in a no longer used pedestrian tunnel under the east-west oriented ridge between Zugspitze and Zugspitzeck (Fig. 1b). Loggers are placed at approximately 2750 m asl and are accessible all year round from the research station Schneefernerhaus (UFS).

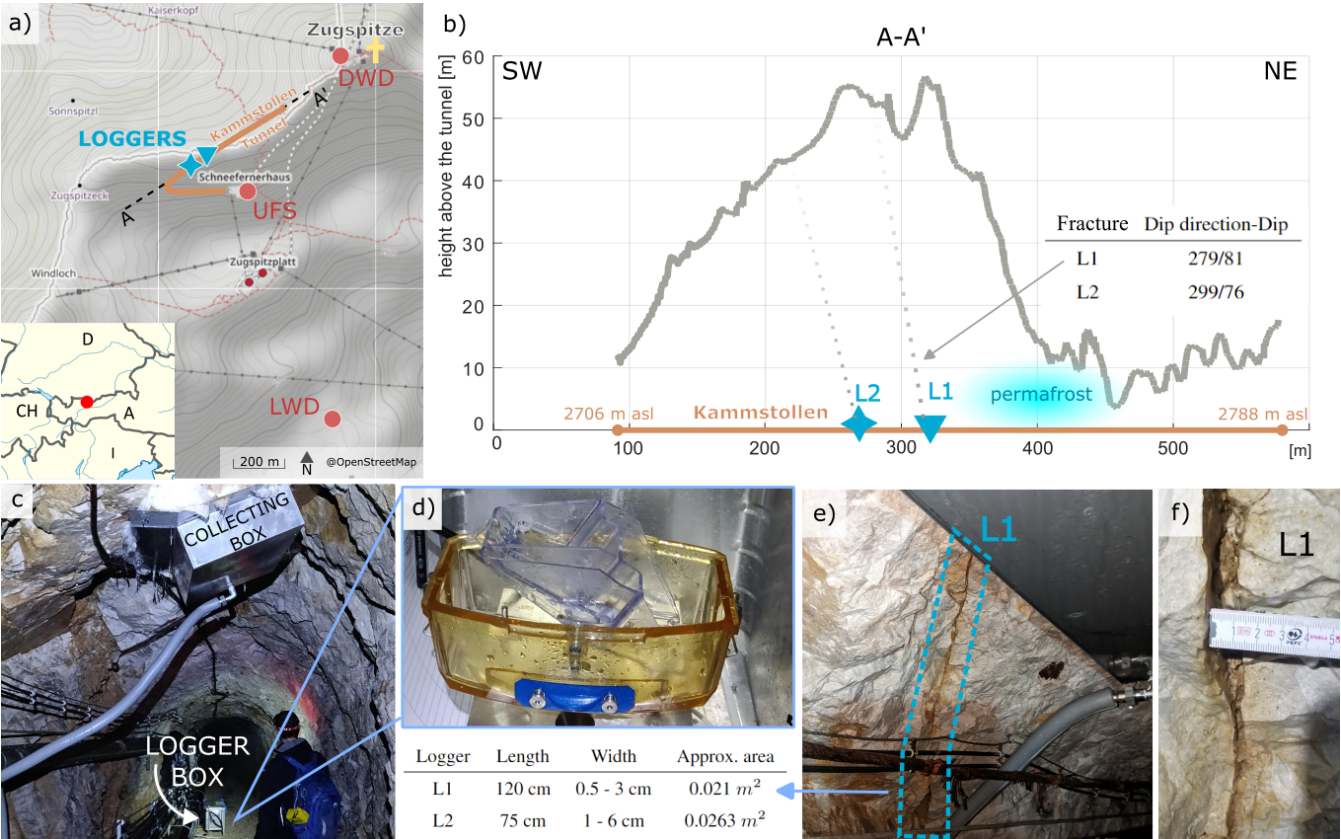


Figure 1. Overview of the study site. a) Inset map: location of the Zugspitze. Main map: summit in yellow, tunnel in orange. Blue signs represent the two flow loggers, and red circles the weather stations: DWD = German Meteorological Service, UFS = Environmental Research Station Schneefernerhaus, and LWD = Bavarian Avalance Service. ©OpenStreetMap contributors 2023. Distributed under the Open Data Commons Open Database License (ODbL) v1.0. b) Section A-A' along the tunnel shows the overlaying rock masses. The table and the dotted lines present the dip direction and dip of the two fractures instrumented with loggers. c) Measuring setup: collecting box, connecting pipe, and logger box. d) Tipping gauge. e) and f) Fracture L1 and detail of it with scale. Table with fractures' dimensions: the fracture area covered by the collecting box is length by width.

2.1 Climate and cryosphere

A long-term meteorological record on the summit (Fig. S1 in the supporting materials) has existed since 1901 by the German Meteorological Service (DWD). The climate is influenced by the prominent elevation at the northern edge of the Alps and by multiple E-W oriented ridges, leading to mean annual precipitation of more than 2500 mm, with no recent changes compared to the reference period. 80% of precipitation is snowfall from autumn to late spring, most parts of the catchment are snow-free at the end of July, and heavy thunderstorms, as well as long-lasting, intense rainfall events, may occur during the summer season (Wetzel et al., 2022). The mean temperature in the last decade (2013–2022) was -3.3°C , which is 1.5°C warmer than the reference period 1961–1990.

Glacier and permafrost degradation in the area has been extensively documented (Mayer et al., 2021; Galleman et al., 2017). A permanently frozen lens has been detected a few decameters from the water loggers (Krautblatter et al., 2010). Monthly geophysical measurements are conducted to monitor its dynamics and identify potential interaction with infiltrating water.

2.2 Hydrology

The basin south of the summit, also known as Research Catchment Zugspitze (RCZ, 11.4 km^2), with its high-density sensors network, is one of the best instrumented high-alpine catchments for monitoring hydrological processes (Wetzel, 2004; Weber et al., 2021). Hydrochemical investigations by Rappl et al. (2010) and Weishaupt (2021) provided the catchment borders and their hydrogeological characteristics, defining it as a perfect natural lysimeter. They evidenced a karst water reservoir in the phreatic zone beneath the Zugspitze Plateau that can hold around half of the volume of summer precipitation. During the winter season, from the end of October to April, no karst system recharge occurs, and the outflow spring falls dry (Morche et al., 2008). Because of this dynamic, climate-change-induced variations in the snow cover will strongly affect water availability in the RCZ and in the areas downstream (Weber et al., 2016). Furthermore, Voigt et al. (2021) used relative gravity measurements to detect water storage variations in the RCZ at the catchment scale with promising results. Still, the only known measurements of water discharge in shallow bedrock were conducted for measuring persistent organic pollutants in percolated water (Levy et al., 2017), using the same loggers as in this study.

2.3 Geology and fractures

The whole summit area is composed of Triassic Wetterstein limestone, with a thickness of 600–800 m (Hornung and Haas, 2017). Ulrich and King (1993) report brecciated zones up to 1 m thick that dip steeply (60° – 90°) in the directions of NW–ENE and can be intercalated with ice. A relevant fault zone can be found from above the UFS up to the summit, and karst dissolution is frequent, especially on the Plateau. Krautblatter et al. (2010) mapped the fractures in the tunnel and are here newly analyzed in Figure S2 of the supplementary material. Fractures with a dip of 80 – 90° are the majority (S1, $n=41$) but without a predominant direction ($SD = 90^{\circ}$). The two fractures where the loggers are installed also belong to this group, as confirmed by punctual measurements conducted by Georg Stockinger in 2023 (personal communication). The indoor mapping agrees only partially

with the one from Mamot et al. (2021), which conducted scan lines and field mapping from the surface 400m NW from our site (Fig. S2e). This difference is mainly due to the influence of the fault zone.

3 Data and methods

This section introduces our model’s main components, which are water entering the system (fracture inputs) and water leaving the system (fracture output). Definitions and methods used for analyzing water dynamics are then presented in the last part of this section.

3.1 Fracture input: water from rain and snowmelt

Inputs to the model can be rainfall data from the weather stations or snowmelt data from the software *Snowpack*. The meteorological measurements are conducted at the three locations listed hereafter and in Table 1. For the snowmelt modeling,

| Station | Parameter | Resolution | Time analysed | Usage |
|---------|-----------|-------------|---------------|---------------------------|
| DWD | TA, P | year, month | 1901-2023 | long-term trends |
| UFS | TA, P | 10 Min. | 2000-2023 | rainfall |
| LWD | HS, TA | 10 Min. | 2000-2023 | <i>Snowpack</i> modelling |

Table 1. Metereological data used in this study. Stations: DWD = German Meteorological Service, located on the summit and often influenced by winds; UFS = Environmental Research Station, located at 2650 m asl in the middle of the south slope, is protected from the northern winds but exposed to western atmospheric perturbations; LWD = Bavarian Avalanche Service snow and weather station, located on the plateau at 2420 m asl in a protected and flat position. The exact locations are visible in Figure 1a. Parameters: TA = air temperature, P = precipitation, HS = snow height.

we use the one-dimensional open-source software *Snowpack* (SP), which simulates the evolution of the snow cover based on weather data (Lehning et al., 1999). It reproduces mass and energy exchanges between the atmosphere, snow, and soil and reproduces the evolution of snow microstructure. Simulations are conducted with data from LWD for every hydrological year separately, with 15-minute time steps. The inputs provided are incoming and outgoing shortwave radiation, snow height (HS), relative humidity, air temperature (TA), snow surface temperature, and wind speed/direction. The measured snow depth is a proxy for precipitation inputs to force the mass balance. Data gaps are interpolated with the integrated pre-processing library MeteoIO. Ground temperature is set constant at 0°C, and albedo is estimated based on incoming and reflected shortwave radiation. Boundary conditions for snow melting are adapted each year to fit the melting phase best, but due to model limitations, discrepancies between modeled and measured snow heights are still possible. The most important output is the amount of meltwater [kg/m^2] that leaves the snow cover in liquid form and reaches the ground.

3.2 Fracture output: water discharge from fractures

Two water collecting systems, L1 and L2 (Fig. 1c-d and Fig. S3 in the supplementary material), were installed in 2010 to collect water from two independent fractures (POPALP Report, 2011; Levy et al., 2017). Each system comprises a collecting box installed on the tunnel's ceiling, a connection pipe, and a logger box. Inside this, a tipping bucket with a resolution of 0.1 l, a reed sensor, and a logger record the discharge hourly. The collecting boxes are located in the unfrozen area, as confirmed by electrical resistivities (Krautblatter et al., 2010), and their vertical distance to the surface is ≈ 55 m. The fractures corresponding to each logger and their measures are shown in Figure 1e-f and S3. The UFS has provided discharge data since 2013; new loggers were installed in 2020.

3.3 Analysis of fracture water dynamics

Discharge measurements from snowmelt or rainfall events, meteorological data, and *Snowpack* results are combined in Matlab at hourly and daily resolution. While snowmelt is analyzed seasonally and daily as water flows uninterrupted for many weeks, rainfall is categorized into events as dry periods clearly mark the limits. Mixed events are excluded, whereas rain-on-snow cases in spring are included. An output flow event starts with a sudden increase of the discharge, independent of the starting value, and ends when the flow returns to a value smaller than a threshold (typically 1 l/h). Baseflow is here defined as an almost constant discharge of small magnitude (typically < 1 l/h) that happens after (or before) a flow event and can last up to some weeks, even without further input. In our model presented in Section 5.3, baseflow is closely connected to fracture saturation. By convention, multiple flow events are classified as one if precipitation interruptions are shorter than 24 hours and the resulting hydrograph at the gauges does not reach baseflow status between the two rain events. Input-output anomalies in the flow are detected and analyzed. One example is no-flow events when rain generates no relevant flow in the fracture. The rain events are selected manually and present a high heterogeneity of quantities and duration. Analyses are conducted automatically with a dedicated Matlab function that uses variable parameters provided by the user for each case. All selected events are listed in Figure S7 of the supplementary material, together with the input-output graphics for each event in Figure S8 and S9. The analysis includes 23 rain events from L1 recorded in the last 10 years, while it was possible to detect a relevant flow in only half of the cases for L2 (Tab. S7, supplementary material).

4 Results and interpretation

The first two sections of this chapter evaluate groundwater dynamics of spring snowmelt and summer rainfall separately. The third section then focuses on no-flow events, baseflow, and extreme events, which are crucial for the empirical model.

4.1 Snowmelt induced discharge

Daily (a) and hourly (b) snowmelt in spring 2023 is shown in Figure 2. All seasons are available at daily resolution in the supplementary Figure S4. Figure 3 presents snowmelt statistics from 2013 to 2023.

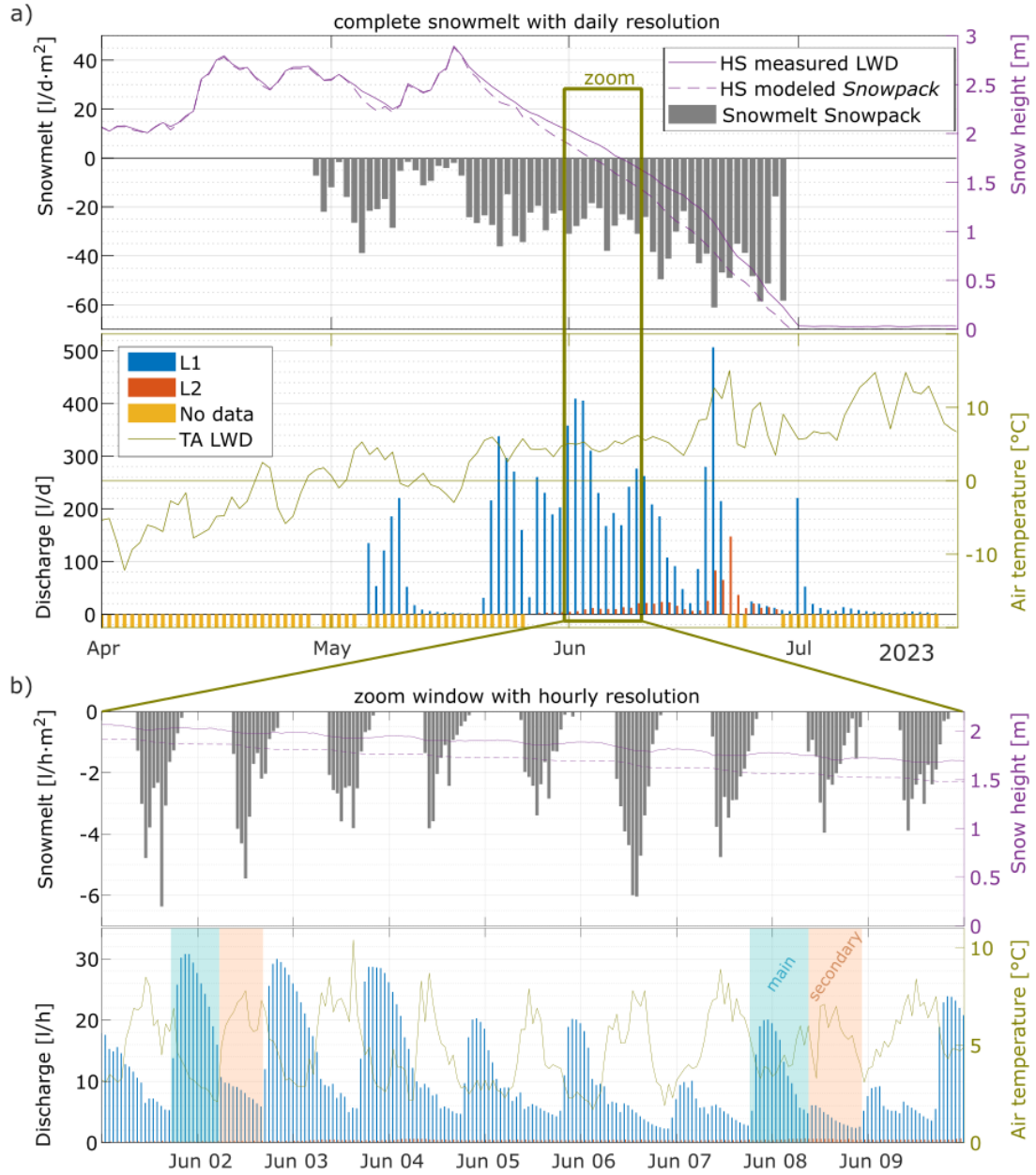


Figure 2. Example of modeled snowmelt rates and measured water discharge for summer 2023, daily rates in subfigure a) and hourly rates in subfigure b). The top panel of each subfigure shows the water input into the rock, i.e., melting water and snow height. The bottom panels show the water output, i.e., the discharge measured in gauges L1 and L2 ($< 1 \text{ l/h}$ in the zoom window), and air temperature. In the bottom panel of b), two different phases of water flow are highlighted: the main flow in blue and the secondary flow in red.

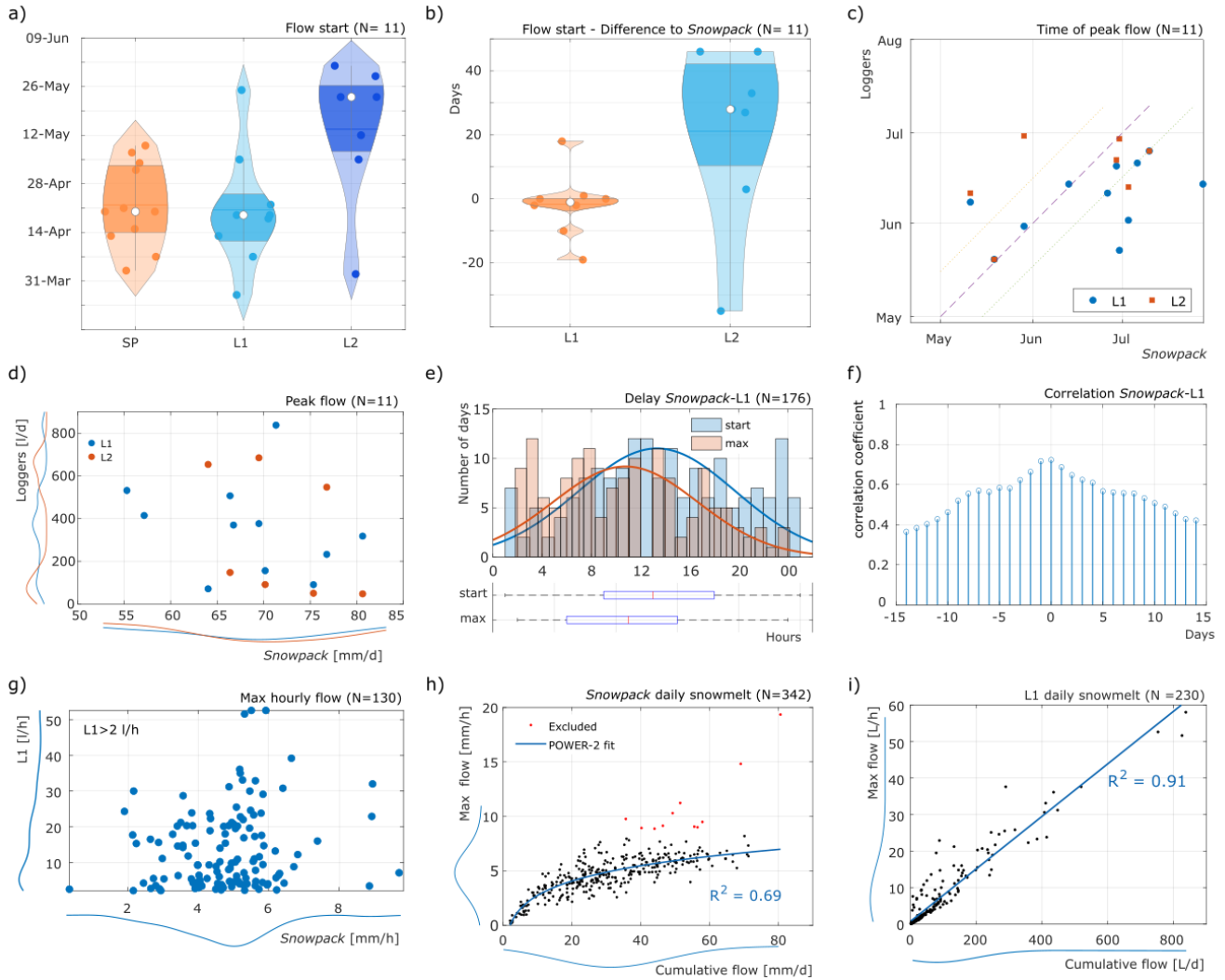


Figure 3. Snowmelt statistics. a) Violin plot of the flow start. The white points represent the median, and the darker areas represent the 25th and 75th percentiles. b) Delay between *Snowpack* (SP) model and fluid flow loggers. c) Time of maximum flow for SP compared to L1 and L2. The line represents the same day. d) Maximum daily discharge for each year for L1, L2 and *Snowpack*, with probability distribution. e) Delay between SP and gauge L1 for flow begin and maximum discharge. f) Daily correlation between SP and L1, with the peak at 0 and -1 days. g) Maximum hourly flow for SP and L1 for each day. h) Maximum daily melting rate and correlated daily cumulative melting for SP. Excluded exceptions mostly represent rain-on-snow events. i) Maximum daily fracture flow and correlated daily cumulative flow for L1.

Seasonal and daily analysis - Snowmelt generally starts at the end of April and lasts until the end of June (Fig. 2a). Small events are also possible in summer or autumn, mostly with negligible quantities. Daily values present good temporal agreement between measurements and *Snowpack* (SP) modeling concerning the starting and the interruptions, but discharge stops earlier

than in the model (e.g., in 2019, 2021, and 2022). The daily modeled melting rates vary across the season: values increase with time, reaching the maximum at the end. The start time of snowmelt is very similar for the model and for L1, while L2 is delayed to the second half of May (Fig. 3a), with a median delay of 28 days from SP (Fig. 3b). Peak snowmelt for SP is mainly at the end of June, while both loggers reach their peak two weeks before or earlier (Fig. 3c). Still, 5 cases show a very good fitting in time. Yearly peak values reach 80 mm/d for SP and 840 l/d for L1, but no correlation between variables is evident (Fig. 3d). The variability of L1 and the fact that, on average, its flow is five times higher than SP can be explained by increased fracture interconnectivity for periods of high flow, so more surface contributes to these events.

Hourly analysis - Figure 2b shows measured and modeled values at hourly resolution. Some disagreements are evident due to water travel time, storage effects, and model limitations. According to SP, snowmelt occurs from 4:00 to 21:00 local time, with a maximum at 13 o'clock and no flow during the night (Fig. S5a in the supplementary material). As expected, melting hours per day increased towards the end of June (Fig. S5b in the supplementary material): this explains the maximum daily melting rates of that period. On the contrary, according to L1 and L2, water flows continuously in the tunnel with daily cycles that vary in intensity and timing over the season, which can be divided into two phases (Fig. 2b). The *main flow* during night hours, marked in blue, and the *secondary flow* during daily hours, marked in red. The superimposition of hydrographs can explain these two flows: water is coming from at least two paths that have different lengths, fracture apertures, and/or filling compositions. The end of an event corresponds to the start of the next: new events mostly start around 12 and have a maximum at 22 o'clock (Fig. S5c). The delay between the beginning of SP melting and water flow increase in the tunnel is 13 h, while the delay between peaks is only 11 h (Fig. 3e), but both show substantial variability. Here, we cannot exclude that the actual delay is a multiple of the calculated one. To verify this, we plotted the correlation between SP and L1 for daily values over 5 years (Fig. 3f and Fig. S6 in the supplementary material). A maximum correlation > 0.7 is reached at 0 and 1 day. Therefore, the delay of peaks can be 11 h or 11+24 h. This variability can be explained by increased fracture interconnectivity or changes in the infill saturation: with high saturation, the hydraulic conductivity increases, and water flows faster. The daily maximum for SP is 4.7 mm/h on average, with a maximum at 9 mm/h, while for L1 is 10 l/h on average, with a maximum at 58 l/h (Fig. 3g and i). No correlation is evident here. The daily cumulative flow of SP does not fit the hourly maximum flow rates linearly (Fig. 3h), while the daily total flow of L1 is linearly correlated to maximum flow rates (Fig. 3i). This is because the quantity of water that can be released by 1 m² of snow during one day is physically limited, but more fractures are connected with higher discharges.

4.2 Rainfall induced discharge

All possible flow trajectories resulting from a rain event are explained in Figure 4. The output discharge from L1 and L2 can differ even with the same input, e.g., in Event 2 (yellow area) a flow is recorded only in L2, indicating different pre-saturation levels in the two fractures. For Event 3, discharge is recorded in both loggers; therefore, both fractures are fully saturated.

Results show that the duration of flow events in the tunnel is mostly longer than precipitation duration (Fig. 5a). Still, the correlation between duration in L1 and L2 is very high (Fig. S10 of the supplementary material). Even short rain events (< 10 h) cause discharges that last longer than two days. There is a sudden increase in flow duration for more prolonged precipitation

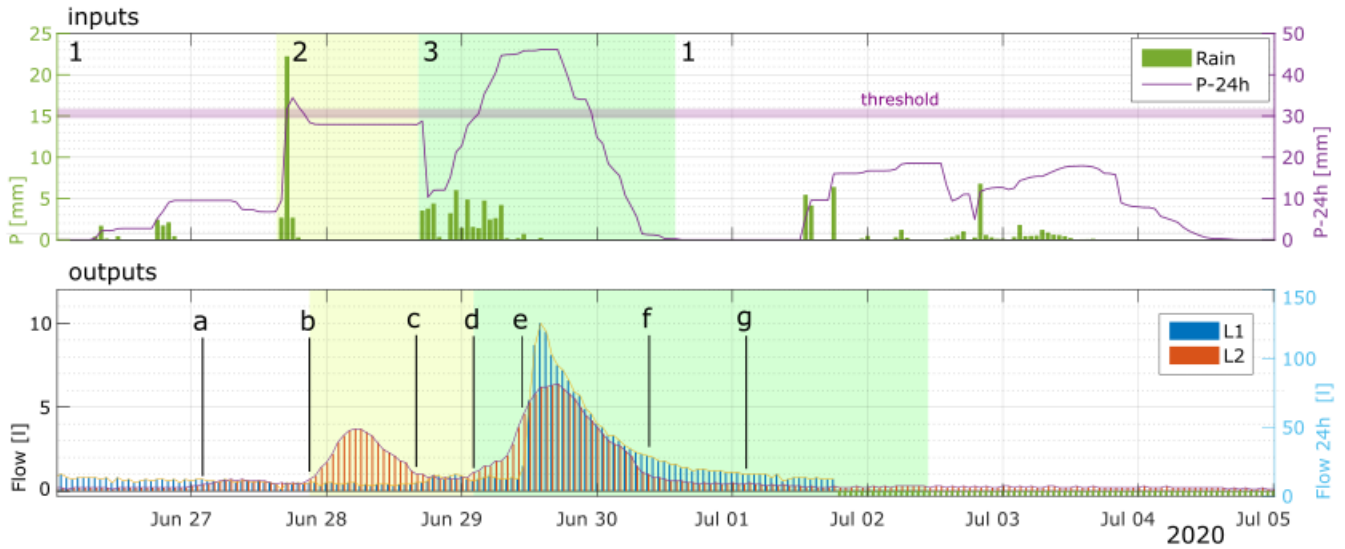


Figure 4. Example of summer precipitation events (i.e., inputs) and the corresponding flow in the fractures (i.e., outputs). Abbreviations: P - hourly precipitation, P-24h - sum of precipitation in the last 24 hours. Upper panel: 1) low-intensity short-duration event with P-24 smaller than the threshold (≈ 30 mm/24 h), 2) high intensity-short duration event around the threshold, and 3) low-intensity long-duration events with P-24 above the threshold. Lower panel: L1 in blue and L2 in red. a) L1: no changes, L2: increase of baseflow, b) L2: begin of event, c) L1: increase of flow, d) L2: begin of the second event, e) L1: beginning of the first event, f) L2: end of the event, only baseflow, g) L1: inflection point, end of the event, only baseflow.

175 (> 80 mm), which also points to an increase in fracture interconnectivity. Flow in the gauge L1 can last up to 7 times longer than the precipitation (Fig. 5f). The delay from precipitation start to flow in the tunnel is 31 h for both loggers (Fig. 5b), but this time can vary ± 10 h according to the amount of precipitation occurring in the previous 3 days (Fig. 5c). This value is a good proxy for the pre-saturation level of the fracture: the more rain before the event, the higher the fracture's saturation, so the faster the water flows. Maximum hourly flow rates in L1 (3.9 l/h) are smaller than precipitation (8 mm/h) due to slow percolation smoothing the peaks (Fig. 5d), but if we consider the 24h-sums, the discharge in the tunnel becomes proportionally larger than the precipitation (Fig. 5f and Fig. S10). Total quantities confirm this: more than one liter of water reaches the tunnel for each mm of rain falling on the surface: 2.3 l/mm of rain in L1, 1 l/mm for L2 (Fig. 5e). These values can be converted in m^2 and express the minimum catchment size for the fractures: considering losses by evaporation and superficial runoff, we can suppose that, in reality, larger areas contribute to each fracture. No events are recorded in the tunnel with less than ≈ 30 mm precipitation (Fig. 5e).

180

185

4.3 No-flow and extreme events

No-flow - Rain events that do not produce a relevant water flow in the tunnel are hereafter defined as no-flow events. We selected 49 summer rain events to investigate this anomaly (Tab. S2, supplementary material). No-flow events have maximum

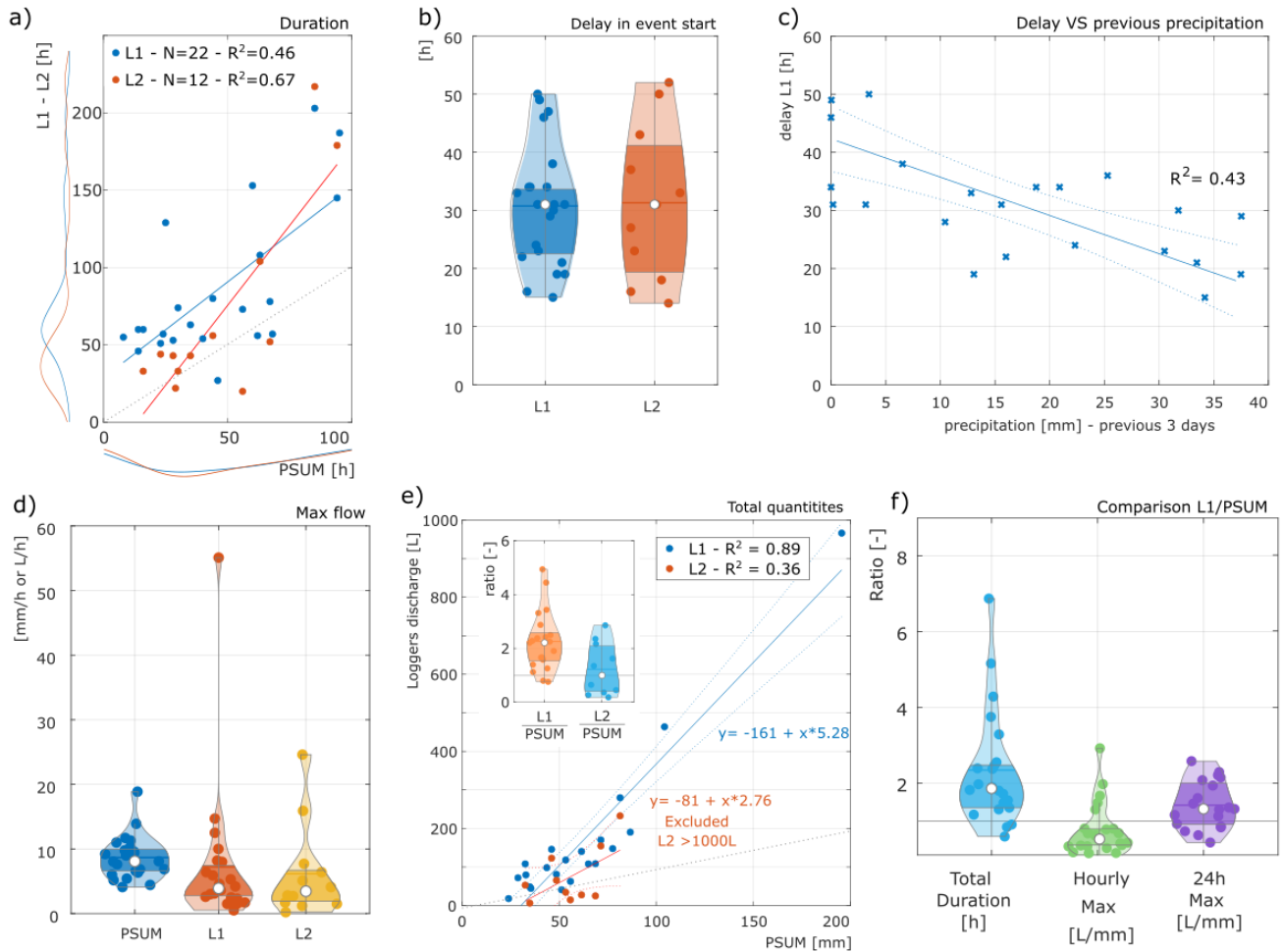


Figure 5. Analysis of rain events. a) Correlation for event duration: P compared to flow in L1 and L2. b) Violin plot of the delay between precipitation and flow in L1 and L2. c) Relation between precipitation in the three days before the event and delay for L1. d) Violin plot with maximum hourly precipitation and flow rate. e) The main graph shows the correlation analysis for the total quantities, L1 or L2 vs. P. The small graph shows the ratios L1/P and L2/P for total quantities. f) Ratios L1/P for different quantities: event total duration, maximum flow rate, and 24h-cumulative maximum flow.

precipitation of ≈ 34 mm and last up to 36 h. Still, the 6h-precipitation is very similar to the total precipitation, meaning that the precipitation is mostly concentrated in a few hours. Total precipitation and peak intensity are poorly correlated with duration (Fig 6b), but total precipitation is related to the peak intensity (Fig 6c), confirming the predominance of short high-intensity rainfalls, likely thunderstorms. This is further supported by the absence of no-flow events that exhibit long durations and low intensities.

Extreme events - The logger recorded two special cases with extreme discharges. The first is the snowmelt on 10th-12th June 2019, which happened after a record snow depth of more than 6 m in May, coincidentally with a sudden increase in air temperature up to +10°C. This caused extreme tunnel discharges up to 800-750 l/d for three consecutive days. The second extreme event is the rainfall on 16th-18th July 2021, with peak intensities of 160 mm/ 24 h and 20 mm/h, preceded by multiple smaller rain events in the five days before, which pre-saturated the fractures. This event was forecasted by the public warning service and generated floods in the valley. In the tunnel, discharges reached values above 800 l/d and hourly values up to 55 l/h, the maximum in the last 10 years. In this case, the delay between peak precipitation and peak flow was only 3 hours.

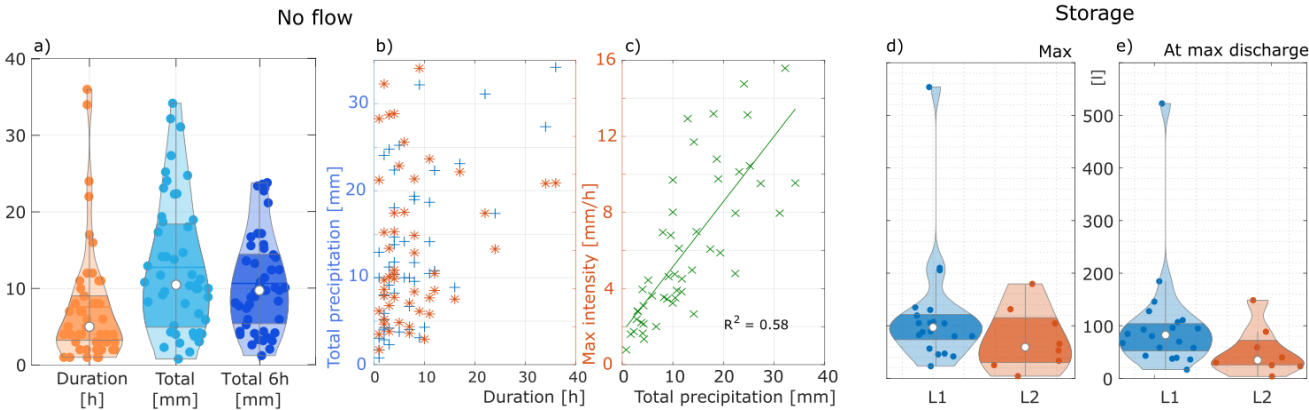


Figure 6. Analysis of no-flow events and storage a) Statistics and spread for 49 events. b) Correlation between duration and total precipitation (blue crosses) or maximum intensity. c) Correlation between total precipitation and maximum intensity. d) Maximum storage and e) storage at maximum discharge.

5 Modelling flow and storage in deep-bedrock fractures

In the following section, we compute the recession curve and analyze flow anomalies. Afterward, we explain the anomalies by introducing the empirical model for fracture saturation and quantifying stored quantities. Finally, discharge values are used to estimate hydraulic heads. The following analyses focus solely on rain events because they are distinctly separated by dry periods, and all input/output quantities are directly measured and, therefore, are highly reliable.

5.1 Recession-curve fitting

Recession curves can fully reproduce discharge behavior using empirical coefficients. These aquifer intrinsic parameters provide information on the flow characteristics and on the attributes of the aquifer, e.g., estimation of karstification degree (Malík and Vojtková, 2012; Kirchner, 2009). Boussinesq (1877) was the first to describe aquifer drainage and spring discharge through a porous medium using a diffusion equation. Using simplifying assumptions, he obtained the approximate analytical solution

described by Equation 1, similar to Maillet (1905) for reservoir emptying through a porous plug.

$$Q_t = Q_0 e^{-\alpha t} \quad (1)$$

Here Q_t is the discharge at time t , Q_0 is the initial discharge, and α is the recession coefficient. Other equations are available to better fit various shapes of hydrograms, e.g. linear equations. Complex aquifers with mixed laminar-turbulent flow regimes, like karst with multiple conduits, require more equations to fully reproduce their groundwater circulation (e.g., Eq. 2).

$$Q_t = \sum_{i=1}^n Q_{0i} e^{-a_i t} + \sum_{i=1}^m Q_{0i} (1 - \beta_i t) \quad (2)$$

We first analyzed all events in L1. Normalized curves show a similar pattern (Fig. S11 and S12 of the supplementary material) with a discharge peak after only 10% of the time. Later, at 40% of the time, discharge decreases back to 30% of the peak, and the remaining 60% of the time is required to return to baseflow. For the recession-curve fitting, we extracted the discharge part from all events and divided multiple peaks into sub-events, with one curve for each peak. All the curves are first plotted at time $t = 0$ (Fig. 7a) and then, starting from the biggest values, each curve is shifted in time so that its starting value fits the same value of bigger events (Fig. 7b). Finally, we computed the mean of the shifted curves and tested different fitting solutions for it (Fig. 7c), according to Malík (2015). The best results for our spring are obtained using Equation 2 with $n = 2$ and $m = 0$ (Fig. 7d), which reduces the error to an acceptable level (Table S1 in the supplementary material). According to the classification suggested by Malík and Vojtková (2012), "the combination of two or more sub-regimes with merely laminar flow (*exponential equations*) characterized by higher values of α " describes a flow happening in an "irregularly developed fissure network, with the majority of open macrofissures, and with the possible presence of karst conduits of limited extent".

5.2 Flow anomalies detection

Combining input on the surface and output in the tunnel, we observe situations where the presence or absence of water in the tunnel can not be directly explained. These unforeseen flow behaviors are analyzed in Figure 8, and all are explainable by water accumulation in the bedrock above the tunnel ("storage"). Possible storage includes (i) karst voids, (ii) pores, and (iii) fractures. i) Results of the recession curve confirm that the presence is possible but only to a limited extent. Extensive karst voids are present under the Plateau (Wetzel, 2004), but their presence in our study area has not been proven yet. Therefore, we exclude this possibility. ii) An average rock matrix permeability of $5 \mu D$ (Krautblatter, 2009) strongly limits the storage possibilities in the matrix. iii) Fractures are preferred flow paths and can temporarily store water due to their filling with fine material. Therefore, our model will focus on this component.

5.3 Fracture saturation and storage model

Figure 9 presents the empirical model that explains flow anomalies. The model is composed of four stages and allows a qualitative forecast of the saturation level in the fracture: from unsaturated (S1) through partially saturated (S2a and S2b) to fully saturated (S3). S2a and S2b differentiate for the outflow: in S2a, we have no flow, while in S2b, we have baseflow. Discharge

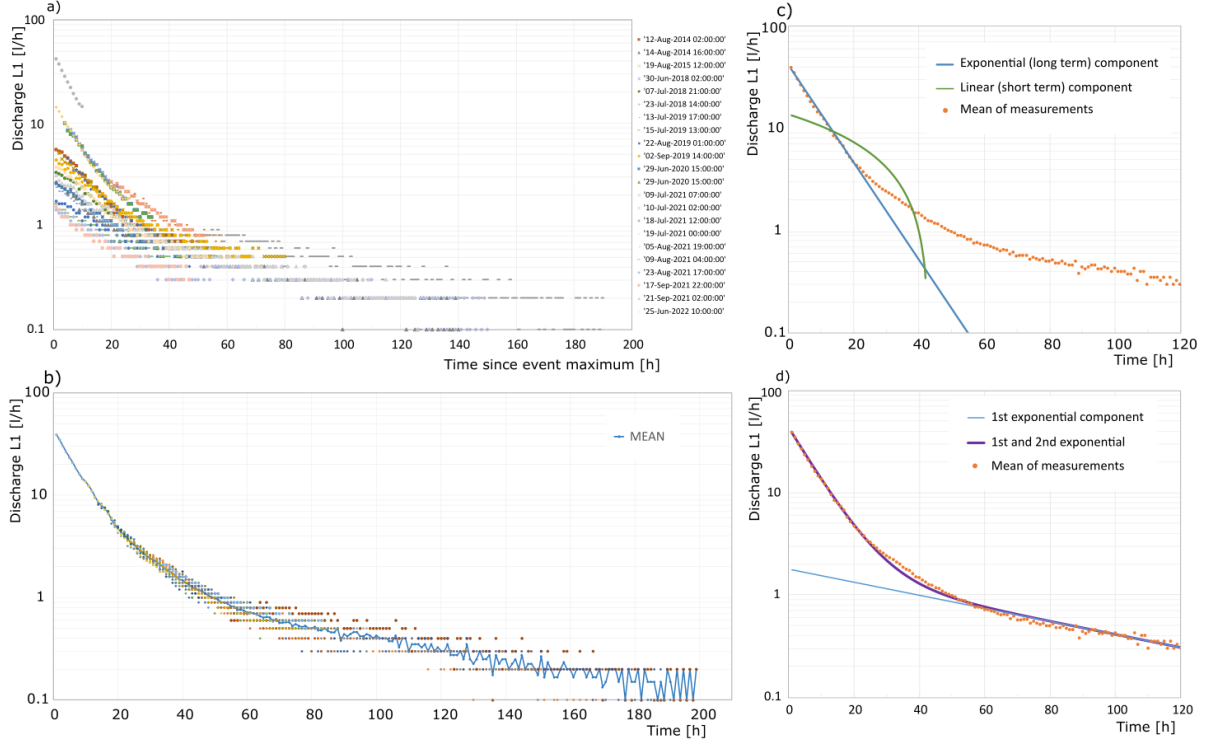


Figure 7. Modelling of all discharge events with a uniform recession curve. a) All events are plotted with $t_0 = 0$ and semi-logarithmic axes. b) Discharge curves are shifted in time so that Q_0 fits a similar value from a higher curve. In blue is the mean curve. c) Recession curves fitting with single equation linear flow component (green line) and single equation exponential flow (blue line). d) Recession curve fitting with 2-components exponential flow.

in the tunnel happens when fractures are fully saturated (S3). S2a/b and S3 can alternate repeatedly when precipitation events happen in quick succession. During dry periods, when S1 resumes, and baseflow reduces to zero, we suppose the fracture to be unsaturated, as in Sweetenham et al. (2017).

This model allowed us to estimate the amount of water stored in the fractures at each time step. For this, we calculated the cumulative discharge Q [l] and precipitation P [l/m²] at the end of the event. While the first is exactly known, the exact amount of rain infiltrating the fracture is unknown. Therefore, for each event, we calculated the ratio R_{end} (Eq. 3), which is the surface required to obtain the discharge measured in the tunnel. This value represented only a minimum estimation since we excluded superficial runoff and evaporation.

$$R_{end} = \sum_{t=0}^{end} Q_t / \sum_{t=0}^{end} P_t \quad (3)$$

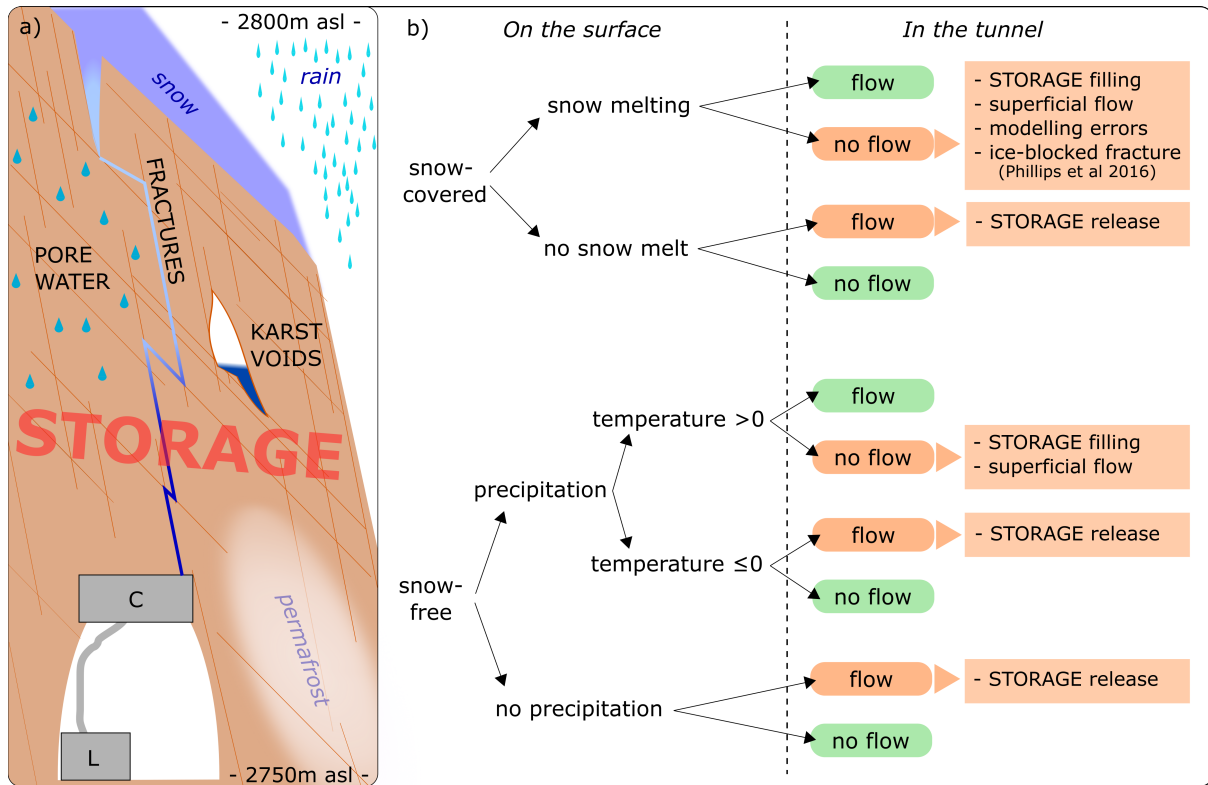


Figure 8. Flow anomalies detection. a) Simplified model of all hydrological components. Storage includes fractures, karst voids, and pores, i.e., all locations where water can accumulate. In the tunnel, we find the collecting box (C) and the logger (L). b) Analysis of water presence: green boxes show expected situations, while orange boxes highlight unexpected situations with possible explanations. All these cases can be explained by water accumulation in the bedrock.

250 R_{end} was then used in Equation 4 to determine the difference between cumulative input and output at each time step t , which corresponds to the storage level S_t .

$$S_t = \sum_0^t P_t * R_{end} - \sum_0^t Q_t \quad (4)$$

The supplementary material presents the storage curves for all events in Figure S13 and S14. The average storage in the fracture system is 97 l for L1 and 59 l for L2 (Fig. 6d).

255 Considering that the timing of the maximum storage is different from the time of maximum discharge in the tunnel (see points A and B in Fig. 9), we expect the maximum pressure in the fracture when the maximum discharge is recorded. Here, we also suppose that all the water in the fracture is concentrated at one point, which is the bottleneck of the fracture. Storage reduces by 15-20% from A to B, and the maximum storage at B reaches 520 l in July 2021 (Fig. 6e).

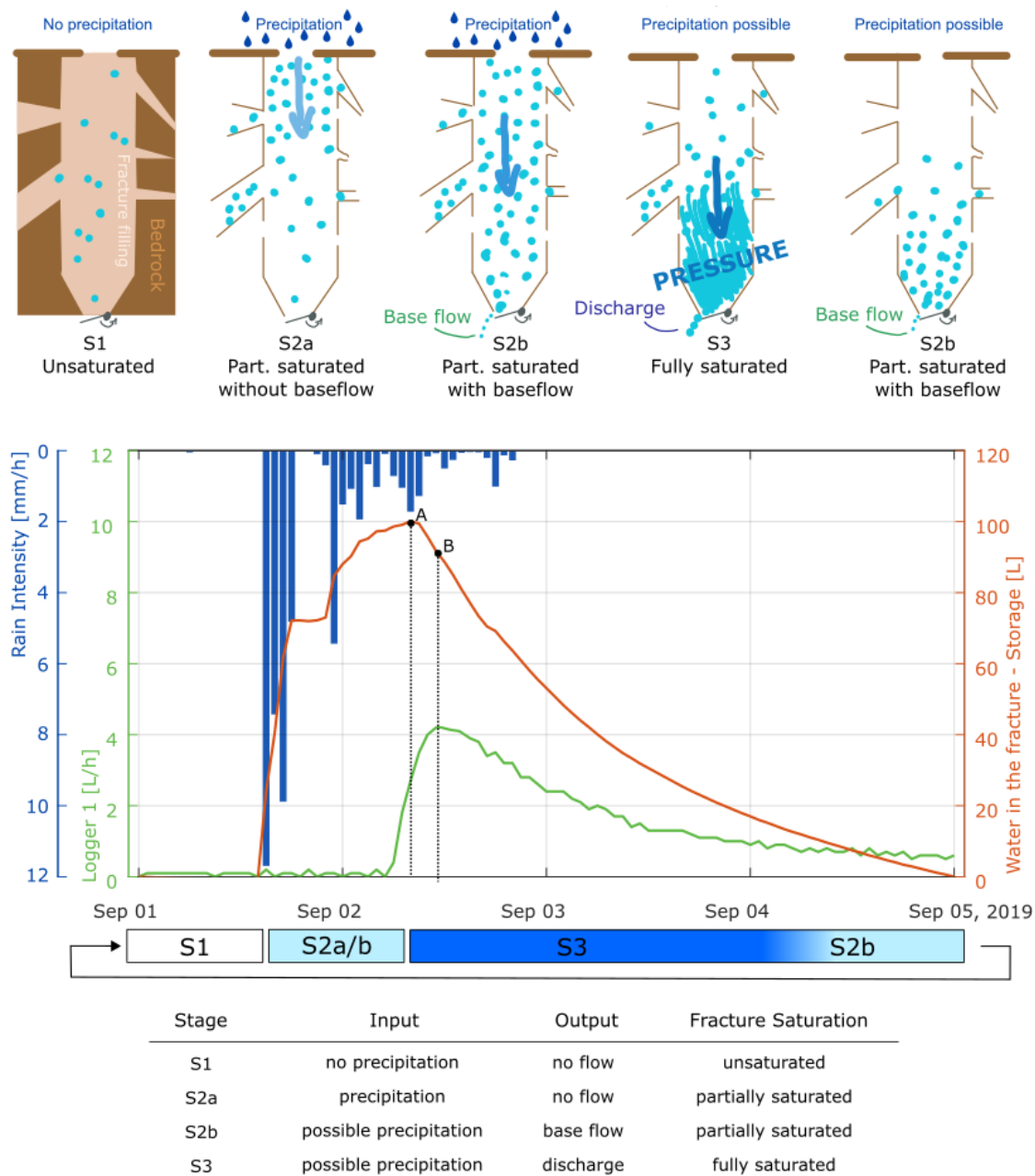


Figure 9. Fracture saturation and storage model. Upper image: graphical representation of the four phases of the model. Central graph: exemplary summer rainfall event. Precipitation (blue bars), fracture discharge (green line), and the corresponding storage level from Eq. 4 (red line). Point A represents the maximum storage in the fracture system, and point B represents the storage at maximum discharge. Lower table: stages of the fracture saturation model as a consequence of input and output.

260 5.4 Estimating hydrostatic pressures from discharge

Finally, we estimated the resulting hydraulic head using Darcy's Law (Eq. 5), the basic equation that describes fluid flow through saturated porous media.

$$q = -K \frac{\Delta h}{\Delta l} \quad (5)$$

265 Here, q is the specific discharge [LT^{-1}], K is the hydraulic conductivity [LT^{-1}], h is the head [L], and l is the travel distance [L] (Zha et al., 2019). According to Bernoulli's equation (Eq. 6), the total hydraulic head h_t can be composed of elevation head h_z , pressure head h_p , and velocity head h_v . In this case, h_v can be neglected due to extremely low velocities in porous media, and h_p should be constant within the system. Therefore, the elevation head h_z is the dominant component, and it drives water flow (Allan Freeze and Cherry, 1979).

$$h_t = h_z + h_v + h_p \approx h_z \quad (6)$$

270 To constrain the hydraulic head, we compared our case to a falling-head test with a Darcy cylinder as in Figure 10a and made the following four assumptions. i) The only constant head is at the discharge point. ii) The diameter is constant over the whole length ($a = A$, in Fig. 10b). iii) L is the "effective path" that offers hydraulic resistance; therefore, a hydraulic head can build up above it. iv) Lateral flow is neglected.

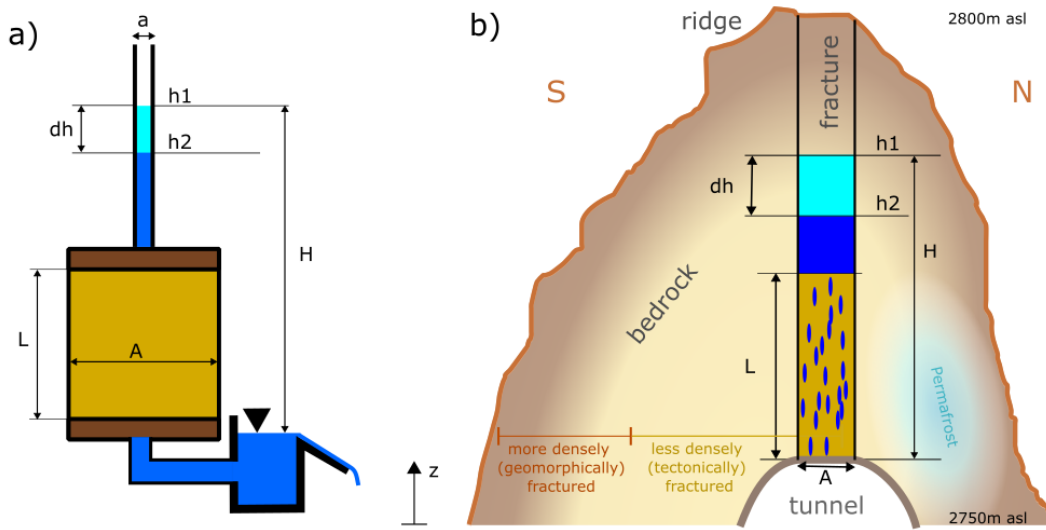


Figure 10. Application of Darcy's Law for a falling head. a) Darcy cylinder with falling head in the pipe above it and constant head at the outflow. b) Illustrative S-N transect of the fracture for water flow with falling head. Bedrock deeper than 8 meters is expected to be less densely fractured (Clarke and Burbank, 2011).

In Figure 10a, the discharge according to Darcy is $Q = q \cdot A = -K \cdot H/L \cdot A$ and it must be equal to the change in hydraulic head, i.e., the discharge rate above the effective path $Q = a \cdot dh/dt$.

$$a \frac{dh}{dt} = -KA \frac{h}{L} \quad (7)$$

Since here $a = A$, we can simplify, rearrange the terms, and integrate the equation, obtaining:

$$\int_{h_1}^{h_2} \frac{dh}{h} = -\frac{K}{L} \int_{t_1}^{t_2} dt \quad \ln(h_2) - \ln(h_1) = -\frac{K}{L}(t_2 - t_1) \quad (8)$$

Solving for the maximum event length, we suppose $t_1 = 0$, and $t_2 = t_{max}$ is obtained from the recession curve. Considering baseflow at the end ($h_2 = 0.1$ m), we can compute the hydraulic head at the beginning (h_1).

$$h_1 = 0.1 \cdot e^{(K \cdot t_2/L)} \quad (9)$$

The following boundary conditions apply in this case.

- i) The height of the surface above the tunnel: $h_1 < 55$ m.
- ii) Bedrock porosity, including matrix and fractures, is estimated at 2.5 ± 1.5 % (Krautblatter, 2009), which gives an average storage capacity of 25 ± 15 l for each m^3 of rock. Considering the extreme event of July 2021, 520 l must be stored above the tunnel, resulting in $13 < h_1 < 52$ m. These numbers might be smaller since, on the surface, porosity and fractures increase.
- iii) The length of the *effective path*, L , must be realistic: $5 < L < 20$ m. We fix one value for the whole process.
- iv) The theoretical length of the maximum event (t_2) can be obtained from the recession curve analysis: $t_2 = 200$ h.
- v) A plausible range of hydraulic conductivities is obtained from literature and from the recorded events. According to Allan Freeze and Cherry (1979), K in karst limestone can vary between 10^{-6} and 10^{-2} m/s, while estimated field velocities are $\approx 5 \cdot 10^{-4}$ m/s.

With the given assumptions, these boundary conditions, and Equation 9, we constrained a realistic range for the hydraulic head at the beginning of an event h_1 . First, plausible couples of K and L values were obtained (Fig. 11a and Fig. S3 of the supplementary material). These couples were then validated for different event lengths ($75 < t_2 < 200$ h) in Figure 11b. A realistic value of K appeared to be between $5 \cdot 10^{-5}$ and $1.5 \cdot 10^{-4}$ m/s, we chose the median $1 \cdot 10^{-4}$ m/s, which requires an effective length L between 11.5 and 12.5 m to produce a max hydraulic pressure h_1 between 32 and 52 m. The validation of these results for shorter event duration confirmed their feasibility (Fig. 7b). Each discharge requires a specific time to return to baseflow after an event. This was defined as *time to 0 flow* ($=tt0$), and was obtained for any given discharge Q with Equation 2 and the parameters in Table S1 (Fig. 7c). The resulting values of $tt0$ were used in Equation 9 to compute h_1 (Fig. 11d). This way, we connected discharges from the logger and hydraulic heads in the fracture.

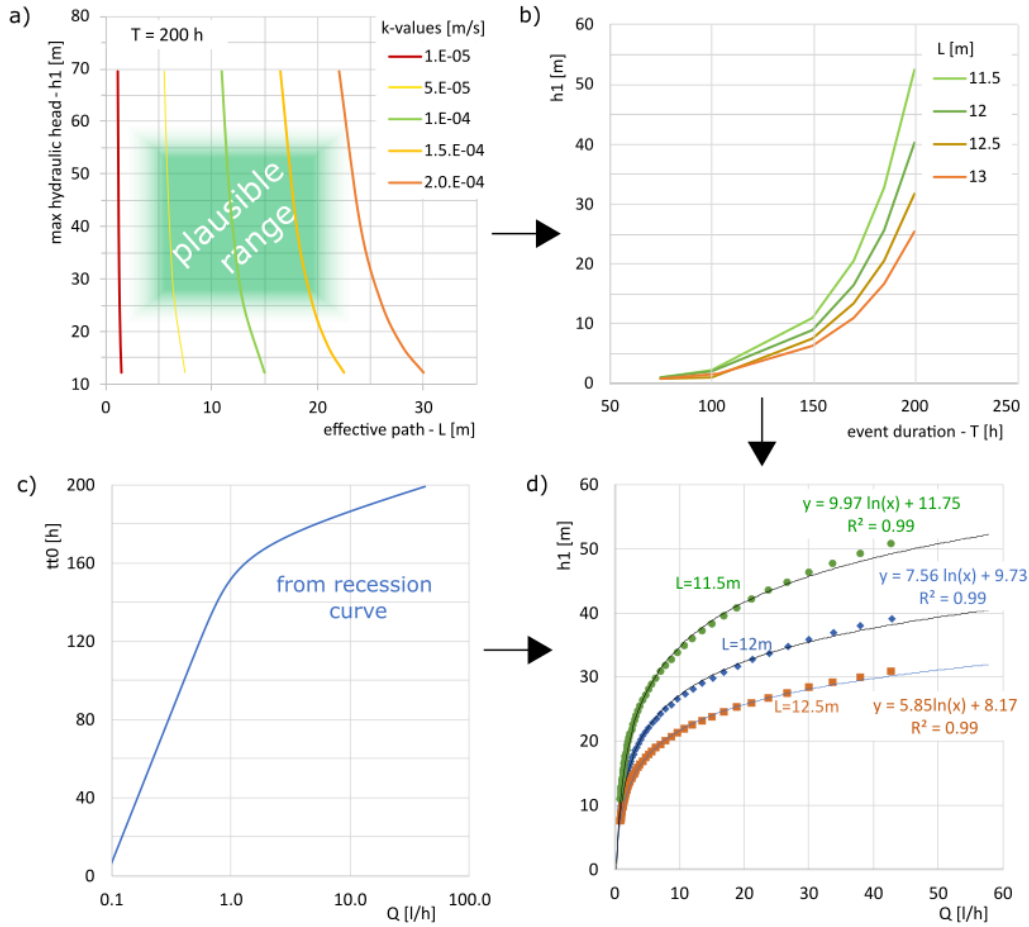


Figure 11. Approximative hydraulic head model. a) Hydraulic head resulting from different effective path (L) and hydraulic conductivity (K). The area in green highlights physically realistic results. b) Validation of the results by changing the event duration. c) Time to 0 flow (tt_0) for each discharge Q . d) Hydraulic head H_1 computed using discharge from fracture L1. For this case, we used $k = 10^{-4} \text{ m/s}$.

Considering the average maximum discharge from the rain events, $Q \approx 4 \text{ l/h}$, a hydraulic head of $20 \text{ m} \pm 4 \text{ m}$ is obtained. For snowmelt, we recorded daily $Q \approx 10 \text{ l/h}$, which generates a hydraulic head of $27 \text{ m} \pm 6 \text{ m}$. Extreme snowmelt in June 2019 could generate a hydraulic head of $40 \text{ m} \pm 10 \text{ m}$ in the fracture, and similar values are also possible for intense rainfall in July 2021.

6 Discussion

This article provides insights into water flow dynamics, reservoir effects, and saturation levels in bedrock fractures. It introduces an empirical method for quantifying hydrostatic pressures generated by snowmelt and rain infiltration. Differently from

previous studies (Scandroglio et al., 2021; Magnin and Josnin, 2021), we don't quantify pressures from model results but
310 based on a decade of high-alpine underground discharge measurements. The robustness of these unique flow data indicates the
occurrence of periods with high water pressure, allowing the following extensive discussion.

6.1 Snowmelt- and rain-driven water flow dynamics in deep fractures as system input

Average and maximum daily infiltration rates from snowmelt are ≈ 30 mm/d and 80 mm/d, respectively, similar to those
measured by Rist and Phillips (2005). The software *Snowpack* can reproduce the timing of extreme melting events but shows
315 disagreement at the end of the melting phase due to the model's poor performance or to the different locations of the snow
station. More snow is available on the flat Plateau compared to the 40/50°-steep slopes, and regular avalanche detachments
for safety reasons further reduce snow availability. A basal ice layer at the cold interface rock-snow is supposed to strongly
limit snowmelt penetration in rock walls (Phillips et al., 2016; Ben-Asher et al., 2023). Still, Kneisel et al. (2014) documented
thermal disturbance in the underground as soon as snowmelt started, while Kristensen et al. (2021) and Roth and Blikra (2009)
320 recorded large increases in rockslide displacements late in the snowmelting season. Our direct flow measurements show that
snowmelt infiltrates every year and that the discharge timing for fracture L1 fits with *Snowpack* modeling from the Plateau,
which lies southward. This suggests that i) the catchment of L1 is on the southern slope and ii) no basal ice layer is blocking
meltwater here. In contrast, a temporary basal ice layer or frozen fractures cannot be excluded for L2, given its delay in some
years. A seasonal basal ice layer could also be present on the steep northern slopes, where snowmelt happens later in the season,
325 as observed during fieldwork.

Summer precipitations reach the tunnel only for events above ≈ 30 mm/24 h. Poulain et al. (2018) confirm that a saturation
threshold is necessary to allow vadose connectivity, although values depend from site to site (Sweetenham et al., 2017). High-
intensity short-duration events like thunderstorms often happen at the beginning of precipitation, generating no-flow or only
baseflow. Most of this water drains away as surface flow due to the total absence of a substrate that acts as a buffer. For the same
330 reason, evaporation effects can be neglected at this location. These effects could influence the estimated storage, so we might
overestimate it. The amount of precipitation in the period before an event influences the travel time of water in the fracture
so that pre-saturated fractures have a higher hydraulic conductivity K . Infiltration rates and fracture conductivity correlate
with fracture patterns at the inlet (Zhou et al., 2006). Therefore, detecting the precise inlet location could further improve the
understanding of the hydrologic system. Unfortunately, the ridge is very exposed, and access is possible only at high risk.

335 6.2 Outflow as the summative system output

The response hydrographs of the two fractures are different: L2 presents a symmetrical hydrograph with similar rising and
falling limbs (Fig. 4d to f), while for L1 the rising limb is very steep. Still, the falling limb has a slow decay (Fig. 4e to g). The
differences could be due to different fracture filling, catchment shapes, isolated karst areas, or higher connectivity. Fracture
density also strongly influences the flow at depth: scarcely fractured networks have a slightly faster response to precipitation
340 than a denser network (Sweetenham et al., 2017). The total annual outflow for L1 reached the decennial maximum value in
2019 with 8500 l/year, which means a theoretical average of 23 l/d. But in that year. One single snowmelt period even recorded

a total of 2300 l in 3 days, which is 27 % of the total, showing that extreme events dominate water dynamics. Measured maximum flow rates are 4 to 10 times higher than those computed by *Snowpack* and measured by Rist and Phillips (2005) because our data are recorded at 50 m depth, where fracture connectivity increases during high discharges (Sweetenham et al., 2017). The highest discharges from snowmelt were recorded at the end of the melting season. For the same period, Weber et al. (2017), Etzelmüller et al. (2022), and Leinauer et al. (2024) demonstrated a clear correlation between snowmelt and increased displacement of unstable slopes. One single rainfall event produced extreme values similar to snowmelt but for a shorter time. A contribution to flow from the neighbor permafrost bodies thaw is theoretically possible. The discharges would be small and visible in dry periods at the end of summer, but it is hard to find signs of it in our data.

350 **6.3 Pressurised water inside fractures as an agent driving slope instabilities**

The computed hydrostatic pressures strongly depend on the selected parameters, although according to our premises, only limited pairs of hydraulic conductivity K and effective length L are reasonable. The presented values are computed for $K = 10^{-4}$ m/s and $L = 11.5$ - 12 - 12.5 m, which are the most likely parameters, but the same results could be obtained using, for example, $K = 5 \cdot 10^{-5}$ m/s and $L = 5.75$ - 6 - 6.25 m. Still, other K - L couples could lead to different hydraulic pressures. Much higher hydraulic conductivities are measured on the Zugspitzplatt by Rappl et al. (2010) with tracers, but this is due to the well-developed karst system present at that location and not at our site.

In extreme cases, hydrostatic pressures up to $40 \text{ m} \pm 10 \text{ m}$ can be reached, similarly to the models of Magnin and Josnin (2021). Average values reach 20 m during summer rainfall events and 27 m during spring snowmelt, pressures that can be mechanically critical (Scandroglio et al., 2021). These levels are achieved many times in the summer season and every day during snowmelt, generating repeated loading-unloading cycles that have been rarely considered but can be a crucial destabilizing factor for slope instabilities. Leinauer et al. (2024) and Helmstetter and Garambois (2010) reported that every drop of water can accelerate or trigger instabilities. This can be true during snowmelt or only for superficial movements since our no-flow measurements and the models of Sweetenham et al. (2017) show that minor rain events do not reach depths of 25-50 m.

The proposed model provides qualitative estimates of fracture's saturation level at depth, which is also crucial for rock wall destabilization (Magnin and Josnin, 2021). When fractures are fully saturated, destabilization acts due to the reduction of cohesion and friction of the fracture's filling material and the reduction of shear strength by counteracting the normal stresses (Scandroglio et al., 2021). During snowmelt, water flows uninterrupted for many weeks, and fractures remain saturated for longer periods. In summer, rain events alternate dry periods, so fracture saturation is highly variable, and destabilizing effects last shortly.

370 **6.4 Error sources and uncertainties**

Error sources and uncertainties are possible in the components of our fracture flow model: the inputs, the outputs, and the estimation of storage and pressure.

Water flow characteristics along the rock fractures

Inputs: Due to the elevation of the study site, the number of snow events ($N > 100$) is larger than the number of rain events

375 (N=23). Snowpack modeling is computed only in 1D at a different elevation than the ridge: 2D or 3D modeling could improve the fitting of the melting phase. Rainfall events are analyzed only hourly, while a 10-minute resolution would provide better insight into high-intensity, short-duration events. Due to their nature, extreme events are rare and statistically less represented. **Outputs:** Both loggers suffered repeated failures due to lightning strikes, battery problems, and maintenance. Therefore, data gaps could be mistaken for no-flow events or for ice sealing the fracture. L1 and L2 don't always behave similarly (e.g.,
380 different discharge hydrographs), but the analyses here focus mostly on L1 because only a few events were recorded by L2. In fact, the latter is more prone to failure and shows variations in peak discharge with time that are not clearly explainable. **Estimation of storage and pressures:** Model calibration took place using one extreme rain event that could present higher K and higher fracture interconnectivity than normal events. To include this variability, all events are incorporated in the recession curve. We chose robust estimates and performed sensitivity propagation to check the robustness of the results. Bedrock deeper
385 than 8 meters is expected to be less densely fractured (Clarke and Burbank, 2011), and a conductivity reduction up to 65% is expected close to a tunnel due to stress increase and joint closure (Fernandez and Moon, 2010). These effects can strongly influence pressure locally (Montgomery et al., 2002). K varies in time according to saturation levels (Fig. 5c), while porosity and hydraulic conductivity are, very likely, not uniform in space. For simplicity, we don't include these variations in our model. Due to the increase of interconnectivity for high discharges, we cannot exclude that in extreme events other than assumed, water
390 spreads laterally and produces hydraulic heads smaller than suggested here.

6.5 Outlook

Snowmelt is expected to begin up to one month earlier by the end of this century (Vorkauf et al., 2021). If so, melting rates will be slower due to the reduced solar radiation early in the year (Musselman et al., 2017), leading to a partial reduction of infiltration rates and consequently lower hydrostatic pressures in fractures during snow-covered periods. Snow-free periods
395 and the number of summer rainfall events might increase. Heavy precipitation will generally become more frequent and more intense with global warming (IPCC, 2023). Accordingly, we expect i) more events with liquid precipitation and ii) more frequent and more intense extreme flow events in fractures, resulting in higher hydrostatic pressures in snow-free periods.

The impact of permafrost bodies on flow paths (Woo, 2012) and water accumulation (Krautblatter et al., 2013) has largely been overlooked. However, climate change is expected to increase active-layer depth, leading to the formation of new hor-
400 izontal and vertical flow pathways. Consequently, the infiltration depth of water will increase, generating higher hydrostatic pressures (Haeberli and Gruber, 2009). Fracture permeability will also be affected since unfrozen fractures are up to three magnitudes more permeable than frozen ones (Pogrebiskiy and Chernyshev, 1977), with significant effects on hydrostatic pressure. Pressurized water in fractures boosts permafrost degradation and could become more important than thermal propagation.

7 Conclusions

405 This study combines a decade of meteorological data, snowmelt modeling, and discharge measurements, thereby providing (i) novel insights into water dynamics in fractured bedrock and (ii) estimating possible hydrostatic pressures.

i) At this elevation, snowmelt produces, on average and in total, higher discharges than rainfall events, but due to climate change, more rain is expected by the end of the century. Extreme events can reach up to 800 l/d from one single fracture. Rainfall reaches the 55m-deep tunnel with an average delay of 31 h, but this value decreases when the fractures are pre-saturated, e.g., during snowmelt periods. No-flow and baseflow events are indicators of unsaturated and partially saturated fractures, respectively. To fully saturate the fractures, more than 30 mm precipitation within 24 h is required, but high-intensity short-duration rain barely contributes to fracture flow. The discharge curves of summer precipitation fit into a general recession curve composed of two exponential terms for laminar flow, which allows forecasting the duration of an event, given its discharge. We detected flow anomalies that can be explained with the help of an empirical fracture flow model, considering saturation changes and water storage. One fracture can store up to 550 l in extreme events, which is expected to fully saturate the fracture and increase its interconnectivity.

ii) The hydraulic head resulting from the water accumulation is computed using the recession curve and Darcy's Law for a falling head. On a daily mean, hydrostatic pressures can reach $27 \text{ m} \pm 6 \text{ m}$ during snowmelt, while rain events generate slightly lower pressures. Snowmelt generates long-lasting pressures with daily cycles that can strongly reduce slope stability. Extreme events produce discharges up to 58 l/h in the tunnel, resulting in hydrostatic pressures of $40 \text{ m} \pm 10 \text{ m}$ (400 kPa). These values are enough to weaken or trigger unstable slopes. Climate change will likely reduce snowmelt pressures and increase summer extreme events.

Here we quantitatively demonstrate the relevance of water flow in deep fractures and prove its relevance for slope stability of degraded bedrock. The estimated hydrostatic pressures can destabilize and/or trigger unstable rock slopes. The combination of climate change and hydrostatic pressures in periglacial areas amplifies permafrost degradation so that in the near future, water is expected to reach new paths and deeper levels, producing higher pressures, thus increasing the hazard.

Code and data availability. Discharge data, modeled snowmelt, precipitation data, and the corresponding codes for data analysis are available at the following online repository <https://doi.org/10.5281/zenodo.13833727> (Scandroglio, 2024). Weather data for snow modeling can be obtained from the Bavarian Avalanche Warning Service (Lawinenwarndienst im Bayerischen Landesamt für Umwelt). Weather data from the summit can be obtained from the DWD German Weather Service at <https://cdc.dwd.de/portal/>.

Author contributions. RS designed the study, performed the analysis, implemented the model, and made the figures in Matlab. RS conducted the fieldwork with the support of TR. RS and SW developed the concept of the study, the data analysis, and the model. RS prepared and revised the manuscript with final approval from all authors. MK supervised the study.

Competing interests. At least one of the (co-)authors is a member of the editorial board of Earth Surface Dynamics. The authors have no other competing interests to declare.

Acknowledgements. This study was supported by the AlpSenseRely project, funded by the Bavarian State Ministry of the Environment and Consumer Protection (TUS01UFS-76976), and by the Hydro-PF project, funded by the TUM International Graduate School of Science and Technology IGSSE (Team 12.9). Special thanks to the Environmental Research Station Schneefernerhaus and the Bayerische Zugspitzbahn Bergbahn AG for the amazing logistic support. We thank all the students and colleagues who provided support in more than 100 days of fieldwork. We are also grateful to Franziska and Thomas from the Bavarian Avalanche Center for the snow data.

References

- Allan Freeze, R. and Cherry, J. A.: Groundwater, Prentice-Hall, 1979.
- Arenson, L. U., Harrington, J. S., Koenig, C. E. M., and Wainstein, P. A.: Mountain Permafrost Hydrology—A Practical Review Following Studies from the Andes, *Geosciences*, 12, 48, <https://doi.org/10.3390/geosciences12020048>, 2022.
- 445 Banks, E. W., Simmons, C. T., Love, A. J., Cranswick, R., Werner, A. D., Bestland, E. A., Wood, M., and Wilson, T.: Fractured bedrock and saprolite hydrogeologic controls on groundwater/surface-water interaction: A conceptual model (Australia), *Hydrogeology Journal*, 17, 1969–1989, <https://doi.org/10.1007/s10040-009-0490-7>, 2009.
- Bast, A., Kenner, R., and Phillips, M.: Short-term cooling, drying and deceleration of an ice-rich rock glacier, *EGUSphere Discussion*, <https://doi.org/10.5194/egusphere-2024-269>, 2024.
- 450 Ben-Asher, M., Magnin, F., Westermann, S., Bock, J., Malet, E., Berthet, J., Ravel, L., and Deline, P.: Estimating surface water availability in high mountain rock slopes using a numerical energy balance model, *Earth Surf. Dynam.*, 11, 899–915, <https://doi.org/10.5194/esurf-11-899-2023>, 2023.
- Boussinesq, M. J.: *Essai sur la theories des eaux courantes.*, Memoires presentes par divers savants a l’Academie des Sciences de l’Institut National de France, tome xxiii edn., 1877.
- 455 Clarke, B. A. and Burbank, D. W.: Quantifying bedrock-fracture patterns within the shallow subsurface: Implications for rock mass strength, bedrock landslides, and erodibility, *Journal of Geophysical Research: Earth Surface*, 116, <https://doi.org/10.1029/2011JF001987>, 2011.
- Courtin, G. M. and Bliss, L. C.: A Hydrostatic Lysimeter to Measure Evapotranspiration under Remote Field Conditions, *Arctic and Alpine Research*, 3, 81, <https://doi.org/10.2307/1550384>, 1971.
- Draebing, D., Krautblatter, M., and Hoffmann, T.: Thermo-cryogenic controls of fracture kinematics in permafrost rockwalls, *Geophysical Research Letters*, 44, 3535–3544, <https://doi.org/10.1002/2016GL072050>, 2017.
- 460 Etzelmüller, B., Czokir, J., Magnin, F., Duvillard, P. A., Ravel, L., Malet, E., Aspaas, A., Kristensen, L., Skrede, I., Majala, G. D., Jacobs, B., Leinauer, J., Hauck, C., Hilbich, C., Böhme, M., Hermanns, R., Eriksen, H. O., Lauknes, T. R., Krautblatter, M., and Westermann, S.: Permafrost in monitored unstable rock slopes in Norway-New insights from temperature and surface velocity measurements, geophysical surveying, and ground temperature modelling, *Earth Surface Dynamics*, 10, 97–129, <https://doi.org/10.5194/ESURF-10-97-2022>, 2022.
- 465 Fernandez, G. and Moon, J.: Excavation-induced hydraulic conductivity reduction around a tunnel – Part 2: Verification of proposed method using numerical modeling, *Tunnelling and Underground Space Technology*, 25, 567–574, <https://doi.org/10.1016/j.tust.2010.04.001>, 2010.
- Fischer, L., Amann, F., Moore, J. R., and Huggel, C.: Assessment of periglacial slope stability for the 1988 Tschierwa rock avalanche (Piz Morteratsch, Switzerland), *Engineering Geology*, 116, 32–43, <https://doi.org/10.1016/J.ENGGEOL.2010.07.005>, 2010.
- Gabrielli, C., McDonnell, J., and Jarvis, W.: The role of bedrock groundwater in rainfall–runoff response at hillslope and catchment scales, *Journal of Hydrology*, 450–451, 117–133, <https://doi.org/10.1016/j.jhydrol.2012.05.023>, 2012.
- 470 Galleman, T., Haas, U., Teipel, U., von Poschinger, A., Wagner, B., Mahr, M., and Bäre, F.: Permafrost-Messstation am Zugspitzgipfel: Ergebnisse und Modellberechnungen, Tech. rep., <https://www.bestellen.bayern.de/shoplink/91115.htm>, 2017.
- Gruber, S. and Haeberli, W.: Permafrost in steep bedrock slopes and its temperatures-related destabilization following climate change, *Journal of Geophysical Research: Earth Surface*, 112, 1–10, <https://doi.org/10.1029/2006JF000547>, 2007.
- 475 Haeberli, W. and Gruber, S.: Global Warming and Mountain Permafrost, *Permafrost Soils*, pp. 205–218, https://doi.org/10.1007/978-3-540-69371-0_14, 2009.

- Haeblerli, W., Wegmann, M., and Vonder Muehll, D.: Slope stability problems related to glacier shrinkage and permafrost degradation in the Alps, *Eclogae geol. Helv.*, 90, 407–414, <https://doi.org/https://doi.org/10.5169/seals-168172>, 1997.
- Hauck, C., Böttcher, M., and Maurer, H.: A new model for estimating subsurface ice content based on combined electrical and seismic data sets, *The Cryosphere*, 5, 453–468, <https://doi.org/10.5194/tc-5-453-2011>, 2011.
- Hayashi, M.: Alpine Hydrogeology: The Critical Role of Groundwater in Sourcing the Headwaters of the World, *Groundwater*, 58, 498–510, <https://doi.org/10.1111/gwat.12965>, 2020.
- Helmstetter, A. and Garambois, S.: Seismic monitoring of Séchilienne rockslide (French Alps): Analysis of seismic signals and their correlation with rainfalls, *Journal of Geophysical Research: Earth Surface*, 115, <https://doi.org/10.1029/2009JF001532>, 2010.
- Hornung, T. and Haas, U.: Erläuterungen zu den Blaettern 8531/8631 Zugspitze und 8531/8632 Garmisch-Partenkirchen, Tech. rep., Bayrisches Landesamt für Umwelt, Augsburg, 2017.
- Immerzeel, W. W., Lutz, A. F., Andrade, M., Bahl, A., Biemans, H., Bolch, T., Hyde, S., Brumby, S., Davies, B. J., Elmore, A. C., Emmer, A., Feng, M., Fernández, A., Haritashya, U., Kargel, J. S., Koppes, M., Kraaijenbrink, P. D. A., Kulkarni, A. V., Mayewski, P. A., Nepal, S., Pacheco, P., Painter, T. H., Pellicciotti, F., Rajaram, H., Rupper, S., Sinisalo, A., Shrestha, A. B., Viviroli, D., Wada, Y., Xiao, C., Yao, T., and Baillie, J. E. M.: Importance and vulnerability of the world’s water towers, *Nature*, 577, 364–369, <https://doi.org/10.1038/s41586-019-1822-y>, 2020.
- IPCC: Weather and Climate Extreme Events in a Changing Climate, in: *Climate Change 2021 – The Physical Science Basis*, pp. 1513–1766, Cambridge University Press, <https://doi.org/10.1017/9781009157896.013>, 2023.
- Jones, D., Harrison, S., Anderson, K., and Betts, R. A.: Mountain rock glaciers contain globally significant water stores, *Scientific Reports*, 8, 2834, <https://doi.org/10.1038/s41598-018-21244-w>, 2018.
- Kirchner, J. W.: Catchments as simple dynamical systems: Catchment characterization, rainfall-runoff modeling, and doing hydrology backward, *Water Resources Research*, 45, <https://doi.org/10.1029/2008WR006912>, 2009.
- Kneisel, C., Rödder, T., and Schwindt, D.: Frozen ground dynamics resolved by multi-year and yearround electrical resistivity monitoring at three alpine sites in the Swiss Alps, *Near Surface Geophysics*, 12, 117–132, <https://doi.org/10.3997/1873-0604.2013067>, 2014.
- Krautblatter, M.: Detection and quantification of permafrost change in alpine rock walls and implications for rock instability, 2009.
- Krautblatter, M., Verleysdonk, S., Flores-Orozco, A., and Kemna, A.: Temperature-calibrated imaging of seasonal changes in permafrost rock walls by quantitative electrical resistivity tomography (Zugspitze, German/Austrian Alps), *Journal of Geophysical Research: Earth Surface*, 115, 1–15, <https://doi.org/10.1029/2008JF001209>, 2010.
- Krautblatter, M., Funk, D., and Günzel, F. K.: Why permafrost rocks become unstable: a rock-ice-mechanical model in time and space, *Earth Surface Processes and Landforms*, 38, 876–887, <https://doi.org/10.1002/esp.3374>, 2013.
- Kristensen, L., Czekirda, J., Penna, I., Etzelmüller, B., Nicolet, P., Pullarello, J. S., Blikra, L. H., Skrede, I., Oldani, S., and Abellan, A.: Movements, failure and climatic control of the Veslemannen rockslide, Western Norway, *Landslides*, 18, 1963–1980, <https://doi.org/10.1007/s10346-020-01609-x>, 2021.
- Lehning, M., Bartelt, P., Brown, B., Russi, T., Stöckli, U., and Zimmerli, M.: SNOWPACK model calculations for avalanche warning based upon a new network of weather and snow stations, *Cold Regions Science and Technology*, 30, 145–157, [https://doi.org/10.1016/S0165-232X\(99\)00022-1](https://doi.org/10.1016/S0165-232X(99)00022-1), 1999.
- Leinauer, J., Dietze, M., Knapp, S., Scandroglio, R., Jokel, M., and Krautblatter, M.: How water, temperature, and seismicity control the preconditioning of massive rock slope failure (Hochvogel), *Earth Surf. Dynam.*, 12, 1027–1048, <https://doi.org/10.5194/esurf-12-1027-2024>, 2024.

- 515 Levy, W., Pandelova, M., Henkelmann, B., Bernhöft, S., Fischer, N., Anritter, F., and Schramm, K. W.: Persistent organic pollutants in shallow percolated water of the Alps Karst system (Zugspitze summit, Germany), *Science of the Total Environment*, 579, 1269–1281, <https://doi.org/10.1016/j.scitotenv.2016.11.113>, 2017.
- Magnin, F. and Josnin, J.: Water Flows in Rock Wall Permafrost: A Numerical Approach Coupling Hydrological and Thermal Processes, *Journal of Geophysical Research: Earth Surface*, 126, <https://doi.org/10.1029/2021JF006394>, 2021.
- 520 Maillet, E.: *Essais d’Hydraulique souterraine et fluviale*, Hermann, Paris, 1905.
- Malík, P.: Evaluating Discharge Regimes of Karst Aquifer, in: *Karst Aquifers—Characterization and Engineering. Professional Practice in Earth Sciences.*, edited by Stevanović, Z., chap. 7, pp. 205–249, Springer, Cham, https://doi.org/10.1007/978-3-319-12850-4_7, 2015.
- Malík, P. and Vojtková, S.: Use of recession-curve analysis for estimation of karstification degree and its application in assessing overflow/underflow conditions in closely spaced karstic springs, *Environmental Earth Sciences*, 65, 2245–2257, <https://doi.org/10.1007/S12665-012-1596-0/TABLES/4>, 2012.
- 525 Mamot, P., Weber, S., Eppinger, S., and Krautblatter, M.: A temperature-dependent mechanical model to assess the stability of degrading permafrost rock slopes, *Earth Surface Dynamics*, 9, 1125–1151, <https://doi.org/10.5194/esurf-9-1125-2021>, 2021.
- Manning, A. and Caine, J.: Groundwater noble gas, age, and temperature signatures in an Alpine watershed: Valuable tools in conceptual model development, *Water Resources Research*, 43, <https://doi.org/10.1029/2006WR005349>, 2007.
- 530 Markovich, K. H., Manning, A. H., Condon, L. E., and McIntosh, J. C.: Mountain-Block Recharge: A Review of Current Understanding, *Water Resources Research*, 55, 8278–8304, <https://doi.org/10.1029/2019WR025676>, 2019.
- Mayer, C., Weber, M., Wendt, A., and Hagg, W.: Die bayerischen Gletscher, die verbliebenen Eisreserven Deutschlands, *Polarforschung*, 89, 1–7, <https://doi.org/10.5194/POLF-89-1-2021>, 2021.
- Montgomery, D., Dietrich, W., and Heffner, J.: Piezometric response in shallow bedrock at CB1: Implications for runoff generation and landsliding, *Water Resources Research*, 38, 10–1–10–18, <https://doi.org/10.1029/2002WR001429>, 2002.
- 535 Morche, D., Witzsche, M., and Schmidt, K. H.: Hydrogeomorphological characteristics and fluvial sediment transport of a high mountain river (Reintal Valley, Bavarian Alps, Germany), *Zeitschrift für Geomorphologie, Supplementary Issues*, 52, 51–77, <https://doi.org/10.1127/0372-8854/2008/0052S1-0051>, 2008.
- Musselman, K. N., Clark, M. P., Liu, C., Ikeda, K., and Rasmussen, R.: Slower snowmelt in a warmer world, *Nature Climate Change*, 7, 214–219, <https://doi.org/10.1038/nclimate3225>, 2017.
- 540 Noetzli, J. and Phillips, M.: *Mountain Permafrost Hydrology*, Tech. rep., WSL Institute for Snow and Avalanche Research SLF, Davos, Switzerland, <https://doi.org/10.16904/slf.1>, 2019.
- Pavoni, M., Boaga, J., Wagner, F., Bast, A., and Phillips, M.: Characterization of rock glaciers environments combining structurally-coupled and petrophysically-coupled joint inversions of electrical resistivity and seismic refraction datasets, *Journal of Applied Geophysics*, 215, 105 097, <https://doi.org/10.1016/J.JAPPGEO.2023.105097>, 2023.
- 545 Phillips, M., Haberkorn, A., Draebing, D., Krautblatter, M., Rhyner, H., and Kenner, R.: Seasonally intermittent water flow through deep fractures in an Alpine Rock Ridge: Gemsstock, Central Swiss Alps, *Cold Regions Science and Technology*, 125, 117–127, <https://doi.org/10.1016/j.coldregions.2016.02.010>, 2016.
- Phillips, M., Buchli, C., Weber, S., Boaga, J., Pavoni, M., and Bast, A.: Brief communication: Combining borehole temperature, borehole piezometer and cross-borehole electrical resistivity tomography measurements to investigate seasonal changes in ice-rich mountain permafrost, *The Cryosphere*, 17, 753–760, <https://doi.org/10.5194/tc-17-753-2023>, 2023.
- 550

- Pogrebiskiy, M. I. and Chernyshev, S. N.: Determination of the permeability of the frozen fissured rock massif in the vicinity of the Kolyma hydroelectric power station, Cold Regions Research and Engineering Laboratory – Draft translation, 634, 1–13, 1977.
- POPALP Report: Erfassung von persistenten organischen Schadstoffen im bayerischen Alpenraum, Tech. rep., München, Helmholtz Zentrum, https://www.lfu.bayern.de/luft/schadstoffe_luft/projekte/doc/schlussbericht_popalp_quellwasser.pdf, 2011.
- Poulain, A., Watlet, A., Kaufmann, O., Van Camp, M., Jourde, H., Mazzilli, N., Rochez, G., Deleu, R., Quinif, Y., and Hallet, V.: Assessment of groundwater recharge processes through karst vadose zone by cave percolation monitoring, *Hydrological Processes*, 32, 2069–2083, <https://doi.org/10.1002/HYP.13138>, 2018.
- Rappl, A., Wetzel, K., Büttner, G., and Scholz, M.: Tracerhydrologische Untersuchungen am Partnach-Ursprung, *Hydrologie und Wasserbewirtschaftung*, 4, 220–230, <http://www.hywa-online.de/landnutzungswandel-und-wasserressourcen-im-bundesdistrikt-zentral-brasilien/>, 2010.
- Rist, A. and Phillips, M.: First results of investigations on hydrothermal processes within the active layer above alpine permafrost in steep terrain, *Norsk Geografisk Tidsskrift - Norwegian Journal of Geography*, 59, 177–183, <https://doi.org/10.1080/00291950510020574>, 2005.
- Roth, M. and Blikra, L. H.: Seismic monitoring of the unstable rock slope at Aaknes, Norway, *Geophysical Research Abstracts*, 11, <https://meetingorganizer.copernicus.org/EGU2009/EGU2009-3680.pdf>, 2009.
- Scandroglio, R.: Collection of data and Matlab-codes for analyzing water dynamic at the Zugspitze., <https://doi.org/10.5281/zenodo.13833727>, 2024.
- Scandroglio, R., Stoll, V., and Krautblatter, M.: The driving force of all nature. Modelling water pressure and its stability consequences on alpine bedrock slopes, *IOP Conference Series: Earth and Environmental Science*, 833, 012 109, <https://doi.org/10.1088/1755-1315/833/1/012109>, 2021.
- Stoffel, M. and Huggel, C.: Effects of climate change on mass movements in mountain environments, *Progress in Physical Geography*, 36, 421–439, https://doi.org/10.1177/0309133312441010/ASSET/IMAGES/LARGE/10.1177_0309133312441010-FIG7.JPEG, 2012.
- Sweetenham, M. G., Maxwell, R. M., and Santi, P. M.: Assessing the timing and magnitude of precipitation-induced seepage into tunnels bored through fractured rock, *Tunnelling and Underground Space Technology*, 65, 62–75, <https://doi.org/10.1016/j.tust.2017.02.003>, 2017.
- Ulrich, R. and King, L.: Influence of mountain permafrost on construction in the Zugspitze mountains, Bavarian alps, Germany, in: International conference; 6th, Permafrost; 1993; Beijing, pp. 625–630, South China University of Technology Press, <https://www.tib.eu/en/search/id/BLCP%3ACN015187124/Influence-of-Mountain-Permafrost-on-Construction/>, 1993.
- van Tiel, M., Aubry-Wake, C., Somers, L., Andermann, C., Avanzi, F., Baraer, M., Chiogna, G., Daigre, C., Das, S., Drenkhan, F., Farinotti, D., Fyffe, C. L., de Graaf, I., Hanus, S., Immerzeel, W., Koch, F., McKenzie, J. M., Müller, T., Popp, A. L., Saidaliyeva, Z., Schaeffli, B., Schilling, O. S., Teagai, K., Thornton, J. M., and Yapiyev, V.: Cryosphere–groundwater connectivity is a missing link in the mountain water cycle, *Nature Water*, 2, 624–637, <https://doi.org/10.1038/s44221-024-00277-8>, 2024.
- Viviroli, D., Dürr, H. H., Messerli, B., Meybeck, M., and Weingartner, R.: Mountains of the world, water towers for humanity: Typology, mapping, and global significance, 43, 7447, <https://doi.org/10.1029/2006WR005653>, 2007.
- Voigt, C., Schulz, K., Koch, F., Wetzel, K.-F., Timmen, L., Rehm, T., Pflug, H., Stolarczuk, N., Förste, C., and Flechtner, F.: Technical note: Introduction of a superconducting gravimeter as novel hydrological sensor for the Alpine research catchment Zugspitze, *Hydrology and Earth System Sciences*, 25, 5047–5064, <https://doi.org/10.5194/HESS-25-5047-2021>, 2021.
- Vorkauf, M., Marty, C., Kahmen, A., and Hiltbrunner, E.: Past and future snowmelt trends in the Swiss Alps: the role of temperature and snowpack, *Climatic Change*, 165, 1–19, <https://doi.org/10.1007/S10584-021-03027-X/TABLES/3>, 2021.

Walter, F., Amann, F., Kos, A., Kenner, R., Phillips, M., de Preux, A., Huss, M., Tognacca, C., Clinton, J., Diehl, T., and Bonanomi, Y.: Direct
590 observations of a three million cubic meter rock-slope collapse with almost immediate initiation of ensuing debris flows, *Geomorphology*,
351, 106933, <https://doi.org/10.1016/j.geomorph.2019.106933>, 2020.

Walvoord, M. A. and Kurylyk, B. L.: Hydrologic Impacts of Thawing Permafrost—A Review, *Vadose Zone Journal*, 15, 1–20,
<https://doi.org/10.2136/vzj2016.01.0010>, 2016.

Watlet, A., Kaufmann, O., Triantafyllou, A., Poulain, A., Chambers, J. E., Meldrum, P. I., Wilkinson, P. B., Hallet, V., Quinif, Y., Van
595 Ruymbeke, M., and Camp, M. V.: Imaging groundwater infiltration dynamics in the karst vadose zone with long-term ERT monitoring,
Hydrol. Earth Syst. Sci., 22, 1563–1592, <https://doi.org/10.5194/hess-22-1563-2018>, 2018.

Weber, M., Bernhardt, M., Pomeroy, J. W., Fang, X., Härer, S., and Schulz, K.: Description of current and future snow processes in a small
basin in the Bavarian Alps, *Environmental Earth Sciences*, 75, 1–18, <https://doi.org/10.1007/S12665-016-6027-1/FIGURES/9>, 2016.

Weber, M., Koch, F., Bernhardt, M., and Schulz, K.: The evaluation of the potential of global data products for snow hydrological modelling
600 in ungauged high-alpine catchments, *Hydrol. Earth Syst. Sci.*, 25, 2869–2894, <https://doi.org/10.5194/hess-25-2869-2021>, 2021.

Weber, S., Beutel, J., Faillettaz, J., Hasler, A., Krautblatter, M., and Vieli, A.: Quantifying irreversible movement in steep, fractured bedrock
permafrost on Matterhorn (CH), *The Cryosphere*, 11, 567–583, <https://doi.org/10.5194/tc-11-567-2017>, 2017.

Weishaupt, S.: *Hochgebirgshydrologie*, 2021.

Welch, L. A. and Allen, D. M.: Hydraulic conductivity characteristics in mountains and implications for conceptualizing bedrock groundwater
605 flow, *Hydrogeology Journal*, 22, 1003–1026, <https://doi.org/10.1007/s10040-014-1121-5>, 2014.

Wetzel, K.: On the hydrology of the Partnach area in the Wetterstein mountains (Bavarian Alps), *Erdkunde*, 58, 172–186, 2004.

Wetzel, K., Bernhardt, M., Weishaupt, S., and Weber, M.: Hydrological investigations in the Wetterstein Mountains at the UFS Schneefern-
erhaus (Bavarian Alps), in: *Science at the Environmental Research Station Schneefernerhaus / Zugspitze*, edited by Bittner, M., chap. 19,
pp. 305–321, 2022.

610 Woo, M. K.: Permafrost hydrology, vol. 97836422234, <https://doi.org/10.1007/978-3-642-23462-0>, 2012.

Zha, Y., Yang, J., Zeng, J., Tso, C. H. M., Zeng, W., and Shi, L.: Review of numerical solution of Richardson–Richards equation for variably
saturated flow in soils, *Wiley Interdisciplinary Reviews: Water*, 6, <https://doi.org/10.1002/WAT2.1364>, 2019.

Zhou, Q., Salve, R., Liu, H.-H., Wang, J. S., and Hudson, D.: Analysis of a mesoscale infiltration and water seepage test in
unsaturated fractured rock: Spatial variabilities and discrete fracture patterns, *Journal of Contaminant Hydrology*, 87, 96–122,
615 <https://doi.org/10.1016/j.jconhyd.2006.05.001>, 2006.